

# **Todo list**

Re-read everything, make sure that the methods for the external noise, burst anlysis of noise and recurrent connections are correct. Double check the convolution methods . . . . .	10
Make sure that the methods for the sodium and potassium variants are correct. LEFT OF HERE, maybe add some numerical information to all the results sections? . . . . .	46

# Exploring Epileptic Neural Dynamics: Insights from a Computational Model of a CA3 Hippocampal Network

Radboud University, Nijmegen

Marc J. Posthuma

26th of April, 2024

# Contents

<b>1</b>	<b>Introduction</b>	<b>5</b>
1.1	Background . . . . .	5
1.1.1	Introduction to Epilepsy and Its Complexity . . . . .	5
1.1.2	Temporal Lobe Epilepsy: A Closer Look . . . . .	5
1.1.3	The Hippocampus and Its Role in TLE . . . . .	5
1.1.4	Functional Brain Networks and Oscillations . . . . .	6
1.1.5	Epileptic States . . . . .	6
1.1.6	Sodium and Potassium Channels in Epilepsy . . . . .	7
1.1.7	Computational Modeling in Neuroscience with NEURON . . . . .	8
1.1.8	Aim of the research . . . . .	8
1.2	Research question . . . . .	9
<b>2</b>	<b>Methods</b>	<b>10</b>
2.1	Computational model . . . . .	10
2.2	Model implementation: cell parameters . . . . .	12
2.3	Model implementation: synaptic connections . . . . .	13
2.4	Model implementation: stimulation and noise . . . . .	15
2.5	Simulations . . . . .	15
2.5.1	Baseline activity . . . . .	15
2.5.2	Model validation . . . . .	16
2.5.3	Sodium and potassium variants . . . . .	16
2.5.4	External noise variants . . . . .	19
2.5.5	External noise: Burst analysis . . . . .	22
2.5.6	Recurrent connection strength variants . . . . .	24
<b>3</b>	<b>Results</b>	<b>26</b>
3.1	Results of the Baseline activity . . . . .	26
3.2	Results of the Model validation . . . . .	28
3.3	Results of the Sodium-Potassium variants . . . . .	34
3.3.1	Firing rates: Pyramidal cells . . . . .	34
3.3.2	Firing rates: Basket cells . . . . .	35
3.3.3	Firing rates: O-LM cells . . . . .	35
3.3.4	Dominant frequencies . . . . .	36
3.3.5	Theta-gamma power . . . . .	37
3.4	Results of the External Noise variants . . . . .	40
3.4.1	Occurrence of depolarization block events across noise conditions	40
3.4.2	Average delay of depolarization block events across noise conditions . . . . .	40

3.5	Results of the External Noise: Burst analysis . . . . .	43
3.5.1	Inter-ictal state . . . . .	43
3.5.2	Pre-ictal state . . . . .	43
3.5.3	Ictal state . . . . .	43
3.6	Results of the Recurrent Connections variants . . . . .	46
<b>4</b>	<b>Discussion</b>	<b>48</b>
4.1	Discussion of the results . . . . .	48
4.2	Implications of the findings . . . . .	48
4.3	Limitations of the research . . . . .	48
4.4	Suggestions for future research . . . . .	48
<b>A</b>	<b>Appendix</b>	<b>49</b>
A.1	Cellular dynamics: equations and parameters . . . . .	49
<b>B</b>	<b>Appendix</b>	<b>53</b>
B.1	Additional tables . . . . .	53
B.1.1	Sodium-Potassium variants numerical results. . . . .	53
B.1.2	Compartment dependent parameters . . . . .	55
B.1.3	Connections . . . . .	56
B.1.4	NetStim parameters . . . . .	58
<b>C</b>	<b>Appendix</b>	<b>60</b>
C.1	Additional data . . . . .	60
C.2	Additional figures . . . . .	60
C.2.1	External Noise variants: DPB percentage matrices . . . . .	61
C.2.2	External Noise variants: DPB delay matrices . . . . .	64
C.2.3	Recurrent connection matrices . . . . .	67

# List of Figures

2.1	Schematic of the CA3 network model . . . . .	11
2.2	Sanjay article results: Figure 6 . . . . .	17
2.3	Depolarization block in basket cells . . . . .	20
2.4	Burst detection example . . . . .	23
3.1	Baseline activity of the CA3 network . . . . .	27
3.2	20 % OLM-Pyr connection scatter plot . . . . .	28
3.3	0 % OLM-Pyr connection scatter plot . . . . .	29
3.4	Validation of the firing rates . . . . .	31
3.5	Validation of the firing rates . . . . .	32
3.6	Validation of the firing rates . . . . .	33
3.7	Sodium-Potassium variants: Firing rates per population . . . . .	34
3.8	Sodium-Potassium variants: Dominant frequencies . . . . .	36
3.9	Sodium-Potassium variants: Theta-Gamma power . . . . .	38
3.10	Comparative FFT of LFP: O-LM variants . . . . .	39
3.11	DPB percentage matrices . . . . .	41
3.12	DPB delay matrices . . . . .	42
3.13	Burst detection near the onset of a depolarization block . . . . .	44
3.14	RC DPB percentage matrices (all) . . . . .	47
C.1	DPB percentage matrices (all) . . . . .	61
C.2	DPB delay matrices (all) . . . . .	64
C.3	RC DPB percentage matrices (all) . . . . .	67

# List of Tables

2.1	Compartment dependent parameters . . . . .	13
2.2	Synaptic Parameters for the Connectivity Between Neurons in the Model . . . . .	14
2.3	Summary of Original Network Simulation Parameters and Results . . . . .	16
3.1	Summary of Model validation: Network simulation Parameters and Results . . . . .	30
B.1	Sodium variant: Pyramidal cell . . . . .	53
B.2	Sodium variant: Basket cell . . . . .	53
B.3	Sodium variant: OLM cell . . . . .	54
B.4	Potassium variant: Pyramidal cell . . . . .	54
B.5	Potassium variant: Basket cell . . . . .	54
B.6	Potassium variant: OLM cell . . . . .	55
B.7	Compartment dependent parameters . . . . .	55
B.8	Synaptic Parameters for the Connectivity Between Neurons in the Model . . . . .	56
B.9	Pyr to Other Cells NMDA Connections Summary . . . . .	56
B.10	Pyr to Other Cells AMPA Connections Summary . . . . .	57
B.11	Bwb to Other Cells GABA Connections Summary . . . . .	57
B.12	OLM to Pyr GABA Connections Summary . . . . .	57
B.13	NetStim Parameters Pyramidal cells . . . . .	58
B.14	Noise to OLM Parameters . . . . .	58
B.15	Noise to BWB Parameters . . . . .	58
B.16	Noise from MS to BWB & OLM Parameters . . . . .	59

# 1 Introduction

## 1.1 Background

In this chapter, the research topic is introduced. The chapter starts with a brief overview of epilepsy, followed by a discussion on the role of the hippocampus in temporal lobe epilepsy. The chapter then discusses the role of the CA3 region of the hippocampus in epilepsy. The chapter then discusses the role of computational modeling in neuroscience. Finally, the chapter discusses the literature gap that this research aims to address.

### 1.1.1 Introduction to Epilepsy and Its Complexity

Epilepsy is a neurological disorder characterized recurrent seizures. Seizures have to be two or more unprovoked and more than 24 hours apart, a single unprovoked seizure with a high recurrence risk ( $>60\%$  over the next 10 years); or the patient needs to have been previously diagnosed with an epilepsy syndrome. Patients with epilepsy usually also suffer cognitive challenges, language difficulties, and an increased risk of mental health issues, such as anxiety and depression (Fisher et al., 2014). At its core, epilepsy involves an imbalance between excitatory and inhibitory processes within the brain. This imbalance can originate in specific brain regions and spread, affecting various interconnected areas outside of the epileptogenic zone (Lüders et al., 2006). The minimum amount of brain tissue of an associated region that initiates a seizure is therefore not fixed and is the reason epilepsy is often thought of as a network disorder.

### 1.1.2 Temporal Lobe Epilepsy: A Closer Look

Temporal Lobe Epilepsy (TLE), the most prevalent form of focal epilepsy in adults, impacts over 50 million people globally. TLE's epileptic events often begin in brain regions like the hippocampus and entorhinal cortex, known for their capacity to independently produce epileptiform activities (Lytton et al., 2005). Despite many TLE patients not responding to medication, research into TLE's underlying mechanisms is vital for developing new treatments.

### 1.1.3 The Hippocampus and Its Role in TLE

The hippocampus, located in the temporal lobe, is crucial for memory formation and retrieval, emotion regulation, and spatial navigation. In TLE, it often serves as the seizure's focal point, especially its CA3 subfield. The CA3 region, with its

dense connections and low epilepsy activation threshold, is particularly susceptible to hyper-excitability (Witter, 2007). Seizures can be triggered by excessive stimulation from higher cortical regions, such as the visual or auditory cortex that project to the hippocampus via the entorhinal cortex in TLE.

#### 1.1.4 Functional Brain Networks and Oscillations

How excessive stimulation is handled however, is dependent on the network's intrinsic properties and its functional connectivity. The CA3 subfield of the hippocampus plays a pivotal role in facilitating higher cognitive function. Perturbations in the connectivity of the CA3 region are common in TLE and directly impacts the working memory (WM) of the network (Arski et al., 2021). However, the exact mechanisms by which these perturbations lead to epileptiform activity are not well understood. The hippocampus is particularly susceptible to connectivity variability which can be transiently induced by epileptic discharge. This is likely due to the high processing demands for WM (Aldenkamp & Arends, 2004).

The neural assemblies that constitute the circuits in the CA3 region are highly regulated and the transfer of information propagates through specific oscillatory patterns. Characteristic neural oscillations in the hippocampus, such as theta (3–12 Hz) and gamma (30–80 Hz) rhythms, play significant roles in forming episodic memory and cognition (Nyhus & Curran, 2010). Epilepsy is associated with alterations in Cross-Frequency Coupling (CFC), where the phase of slower waves modulates the amplitude of faster waves, reflecting disrupted network functionality. Abnormalities in Theta-Gamma Phase-Amplitude Coupling (PAC) correlate with cognitive impairments in epilepsy. Therefore, tracking changes in these neural oscillations can provide insights into the disease's progression.

#### 1.1.5 Epileptic States

Detecting the state of the brain is crucial for predicting and managing seizures, as patients of epilepsy only experience the effects of their disease during seizures. The gold standard of brain activity detection utilizes the electroencephalogram (EEG), which measures electrical fluctuations ranging from  $< 1$  Hz to several kHz.

The associated brain region of an epilepsy patient when investigated can be in one of three states that have been generally defined using various epilepsy detection algorithms. These classification methods extract epileptic features from the EEG based on comparison of different kernels (Linear, Sigmoid, Grid, etc) The classification accuracy of these methods vary but are fairly high ( $>98.9\%$ ) for methods such as Support Vector Machine (SVM) or Wavelet Neural Network (WNN) classification (Yayik et al., 2015).

These general epilepsy states for a patient are defined as follows:

- **Inter-ictal State**

- *Definition:* The period between seizures, with no active seizure activity.
- *Characterization:* Characterized by inter-ictal spikes or sharp waves in EEG. These spikes indicate abnormal electrical discharges that are not actual seizures.

- **Ictal State**

- *Definition:* The period during which a seizure occurs.
- *Characterization:* EEG shows sustained, rhythmic electrical activity distinct from normal or inter-ictal activity, with corresponding behavioral symptoms based on seizure type.

- **Pre-ictal State**

- *Definition:* The period immediately before the onset of a seizure.
- *Characterization:* Marked by subtle and variable changes in EEG and other physiological signals that precede seizures, crucial for seizure prediction efforts.

Identification of the aforementioned states provides a benchmark for potential epileptiform activity in a (simulated) network. Epilepsy as a whole could be viewed particular brain functioning state, manifested in a multi-state network of coupled oscillatory systems. Thus tracking observable phenomena in the CA3 region of the hippocampus, such as bursting or oscillatory coupling could provide insights into the network's susceptibility to ictal transitions (Kalitzin et al., 2019).

### 1.1.6 Sodium and Potassium Channels in Epilepsy

In the past 20 years, research has shown that at least half of all epilepsy cases have a genetic basis. Rapid discovery of disease-causing genes have identified genes encoding for ion channel proteins. Remarkably, a quarter of all cases involving monogenic variants are related to ion channels (Oyrer et al., 2018; Striano & Minassian, 2020). Sodium and potassium channels in particular, are essential for maintaining the resting membrane potential and action potential generation in neurons. Dysfunctional variants of sodium or potassium channels can lead to hyperexcitability in neurons, depending on whether the relevant mutation causes loss or gain of function. This in turn can have destabilizing effects on neural circuits in regions such as the CA3 subfield of the hippocampus in TLE.

A lot of epileptic mutations have been found in *voltage-gated* type ion channel genes. For example, for sodium these are most often related to the brain-expressed SCN family (*SCN1A*, *SCN2A*, *SCN3A* and *SCN8A*, Brunklaus and Lal (2020)). Highly conserved across species, these genes encode for the pore-forming  $\alpha$  sub-units of the sodium channel and are responsible for the fast depolarizing current in neurons. Previous research has shown that mutations in these genes have become increasingly frequent in Mendelian epilepsy syndromes in recent years (Brunklaus & Lal, 2020). These SCN genes are involved in generalized epilepsy with febrile

seizures plus (GEFS+) syndrome. SCN1A in particular encodes predominantly in inhibitory GABAergic neurons, usually enriched in axonal segments and facilitates initiation of action potentials (Yu et al., 2006).

Similarly, there are also common mutations in potassium channels that are associated with epilepsy. The KCNA family genes that encode the respective subunits in potassium channels (*KCNA1* and *KCNA2*, Gao et al. (2022)) are commonly involved in episodic ataxia type 1 (EA1, Graves (2006)). The dysfunction of these channels can lead to hyperexcitability in neurons, which can again lead to a destabilized network.

### 1.1.7 Computational Modeling in Neuroscience with NEURON

The NEURON simulator is a powerful tool for modeling the intricate dynamics of neurons and their networks. It supports detailed simulations of membrane dynamics, synaptic interactions, and the Hodgkin-Huxley model for action potentials. The Hodgkin-Huxley model, a cornerstone of computational neuroscience, describes the ionic currents underlying action potentials in neurons based on non-linear differential equations (Hodgkin et al., 1952).

NEURON's Python interface facilitates scripting and integration with other Python-based tools, enhancing its utility in neuroscience research. This simulator is crucial for studying neural phenomena, the effects of anti-epileptic drugs, and diseases caused by dysfunctional ion channels for sodium and potassium, providing invaluable insights into the functioning of the nervous system and the development of therapeutic strategies (Migliore et al., 2006).

### 1.1.8 Aim of the research

This study aims to further investigate the role of the CA3 region of the hippocampus in epilepsy, by adapting the computational model of the CA3 region of the hippocampus by Neymotin et al. (2011) in the NEURON simulator. The model consists of 800 pyramidal, 200 O-LM interneurons and 200 basket cells. The baseline model contains enough biophysical detail to replicate homeostatic neural activity, consisting of theta-modulated gamma oscillations.

This research builds upon experiments by Sanjay et al. (2015), which focussed on reducing dendritic inhibition, increasing external stimulation and modifying synaptic connectivity as potential causes for TLE.

Instead, this study will focus on the role of sodium and potassium channels via ion-conductance modifications throughout the network, the sensitivity for external noise in such conditions and the effects increasing recurrent connectivity of inhibitory basket cells.

## 1.2 Research question

This research is focused on the following research question:

### Main Research Question

- What is the impact of different genetic profiles on epileptic activity in simulated hippocampal brain circuits?

### Main Hypothesis

- It is hypothesized that by emulating specific genetic profiles within simulated CA3 hippocampal neural networks, we can replicate their impact on the networks' behavior. Furthermore, it is expected that inducing cellular dynamics that reduce seizure-like (ictal) activity will rescue normal network function.

### Investigative Sub-Questions

1. What specific variables characterize (inter)-ictal activity in different neural cell types within temporal lobe epilepsy (TLE) networks?
2. How do these variables vary across different neural networks, and how can they be reliably measured and quantified in a NEURON model?
3. How can genetic variations, such as single nucleotide polymorphisms (SNPs) or known epilepsy-inducing mutations, be successfully integrated into hippocampal neural network models to simulate the impact on ictal activity?
4. What alterations in network dynamics and connectivity patterns are observed when introducing epilepsy-associated genetic variations into neural cell types?
5. Can the effects of specific genetic variants be correlated with the severity and frequency of seizures in the modeled networks?
6. Can we identify specific targets for intervention that can restore normal network dynamics in the presence of epilepsy-associated genetic variations?
7. Are we able to reliably predict the effect of a specific drug on the network dynamics and emulate them in the model?

## 2 Methods

Re-read everything, make sure that the methods for the external noise, burst analysis of noise and recurrent connections are correct. Double check the convolution methods

Make sure that the methods for the sodium and potassium variants are correct.

### 2.1 Computational model

The network model that was used in this research is a custom implementation made by Sanjay et al. (2015). This model is based on the CA3 subfield region of the hippocampus and is implemented in the NEURON simulation environment using python version 3.9.16 as an interface (<https://www.neuron.yale.edu>). The model consists of 1000 neurons, which are divided into populations containing three cell-types: 800 5-compartment pyramidal cells (three apical dendrites, one basal dendrite, and soma), 200 1-compartment soma-inhibiting basket cells and 200 1-compartment Oriens-Lacunosum Moleculare (O-LM) interneurons. The original source code of the model is available on ModelDB at the following link: <http://senselab.med.yale.edu/modedb>ShowModel.asp?model=139421>.

The implementation used in this research made in cooperation with Sean Gies is part of the *Neuromics* software package by Synaptica Ltd. The implementation has been modified to allow for more ease of use and to allow for the implementation of cellular modifications and network manipulations. Descriptions of the cell-types and their classes, network design, synaptic connections and stimulation parameters can be found in appendix A.

The experimental source code for this research project can be found on request on GitHub at the following link: [https://github.com/SynapticaNL/Marc\\_network\\_sims](https://github.com/SynapticaNL/Marc_network_sims).

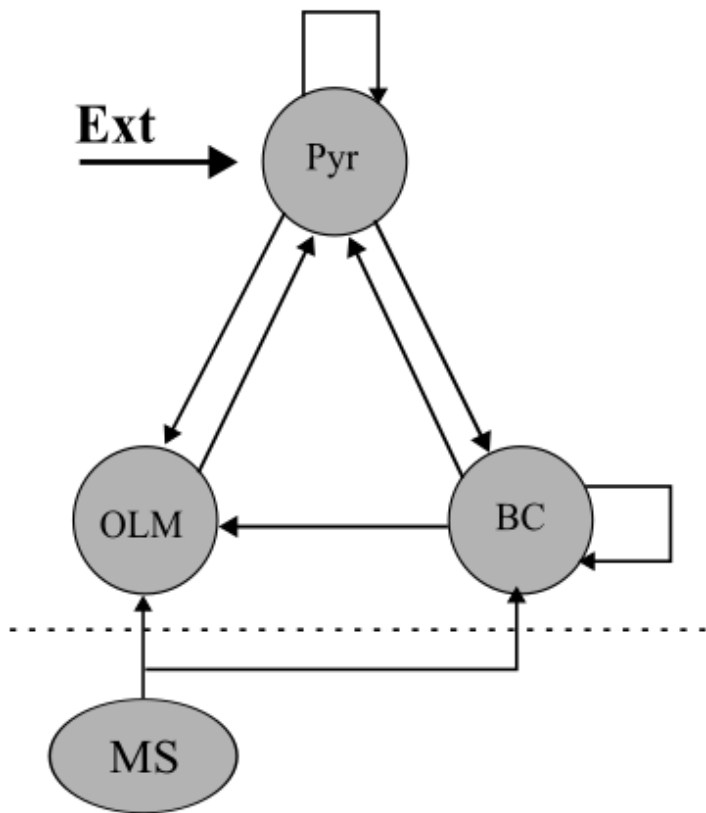


**Figure 2.1:** Schematic of the CA3 network model.

The network comprises of many microcircuits with the connectivity as shown in the above figure. Pyr cells (pyramidal), BC cells (basket cells that inhibit soma), OLM cells (oriens lacunosum moleculare interneurons that inhibit dendrites), external inputs (mainly from the entorhinal cortex) to Pyr cells, and MS (medial septum). BC and OLM cells are stimulated by Pyr cells, while Pyr cells are inhibited by BC and OLM cells. Recurrent connections among Pyr cells are excitatory, whereas those among BC cells are inhibitory. OLM cells are inhibited by BC cells. The medial septum (MS) delivers inhibitory inputs every 150 ms to BC and OLM cells.

## 2.2 Model implementation: cell parameters

The model consists of three types of neurons, each with its own set of parameters and defined cell classes. The parameters for each cell type are based on the following references:

1. **Basket Cells:** Modeled after Wang and Buzsáki (1996), featuring standard dynamics for Na and K currents, along with synaptic and leak currents. Each cell is modeled as a single compartment and obeys the following current balance equation:

$$C_I \frac{dV_I}{dt} = I_{\text{app},I} - I_{\text{Na},I} - I_{\text{K},I} - I_{\text{L},I} - I_{\text{syn},I} \quad (2.1)$$

where  $V_I$  is the membrane potential (mV),  $C_I = 1 \mu\text{F}/\text{cm}^2$  is the membrane capacitance,  $I_{\text{app},I}$  is the applied current, and  $I_{\text{syn},I}$  is the total synaptic current. The leak current  $I_{\text{L},I} = g_{\text{L},I}(V_I - E_{\text{L},I})$  has a conductance  $g_{\text{L},I} = 0.1 \text{ mS}/\text{cm}^2$  and reversal potential  $E_{\text{L},I} = -65 \text{ mV}$ . All currents are in units of  $\mu\text{A}/\text{cm}^2$ . The sodium  $I_{\text{Na},I}$  and potassium  $I_{\text{K},I}$  currents are voltage-dependent spiking currents of the Hodgkin-Huxley type.

2. **O-LM Cells:** Adapted from Saraga et al. (2003), including additional currents like hyperpolarization-activated (h) and A-type currents. Each cell is modeled as a single compartment and obeys the following current balance equation:

$$C_O \frac{dV_O}{dt} = I_{\text{app},O} - I_{\text{Na},O} - I_{\text{K},O} - I_{\text{L},O} - I_{\text{h},O} - I_{\text{A},O} - I_{\text{syn},O} \quad (2.2)$$

where  $V_O$  is the membrane potential,  $C_O = 1.3 \mu\text{F}/\text{cm}^2$  is the membrane capacitance,  $I_{\text{app},O}$  is the applied current, and  $I_{\text{syn},O}$  is the total synaptic current. The leak current  $I_{\text{L},O} = g_{\text{L},O}(V_O - E_{\text{L},O})$  with conductance  $g_{\text{L},O} = 0.05 \text{ mS}/\text{cm}^2$  and reversal potential  $E_{\text{L},O} = -70 \text{ mV}$ .  $I_{\text{Na},O}$ ,  $I_{\text{K},O}$ ,  $I_{\text{h},O}$ , and  $I_{\text{A},O}$  represent the transient sodium, delayed rectifier potassium, hyperpolarization-activated (or h) mixed-cation, and A-type potassium currents, respectively, all in units of  $\mu\text{A}/\text{cm}^2$ .

3. **Pyramidal Cells:** Based on Migliore et al. (2004), incorporating compartmentalized dynamics for the complex morphology of pyramidal neurons. Each cell is modeled as a multi-compartmental neuron with 5 compartments: 1 for basal dendrites (Bdend), 1 for soma, and 3 for apical dendrites (Adend1, 2 and 3). Each compartment obeys the following current balance equation:

$$C_{E_k} \frac{dV_{E_k}}{dt} = I_{\text{app},E_k} - I_{\text{Na},E_k} - I_{\text{K},E_k} - I_{\text{L},E_k} - I_{\text{h},E_k} - I_{\text{A},E_k} - I_{\text{syn},E_k} + I_{\text{conn},E_k} \quad (2.3)$$

where  $V_{E_k}$  is the membrane potential of compartment  $k$ ,  $C_{E_k}$  is the membrane capacitance,  $I_{\text{app},E_k}$  is the applied current,  $I_{\text{syn},E_k}$  is the total synaptic current, and  $I_{\text{conn},E_k}$  represents the current due to electrical coupling between compartments.  $I_{\text{L},E_k}$ ,  $I_{\text{Na},E_k}$ ,  $I_{\text{K},E_k}$ ,  $I_{\text{h},E_k}$ , and  $I_{\text{A},E_k}$  denote the leak, transient sodium, delayed rectifier potassium, hyperpolarization-activated mixed-cation, and A-type potassium currents for compartment  $k$ , respectively.

*For further elaboration of the mathematical formulation of each cell type, see appendix A. For the full overview of cell and compartment parameters, see appendix B.*

## 2.3 Model implementation: synaptic connections

The model contained three types of synaptic connections: excitatory, inhibitory based on AMPA, NMDA and GABA-A receptors. Synapses were modeled by standard NEURON double-exponential mechanism. This approach entailed the assignment of specific rise  $\tau_1$  and decay  $\tau_2$  time constants, which correspond to the temporal profiles of conductance increase and subsequent decline, respectively, following a synaptic event. The conductance values, indicative of synaptic efficacy, were varied according to the type of presynaptic and postsynaptic neuron pairing, as well as the subtype of receptor involved (AMPA, NMDA, or GABA-A). These parameters informed the simulation of synaptic inputs, which govern the depolarization and hyperpolarization events in the postsynaptic neuron membrane, thereby influencing the temporal patterns of neuronal firing and network activity. These parameters adhere to the following formula:

$$g(t) = \frac{g_{\max}}{\tau_2 - \tau_1} \left( e^{-\frac{t}{\tau_2}} - e^{-\frac{t}{\tau_1}} \right) \quad (2.4)$$

The synaptic conductance at a given time  $t$  after a presynaptic spike is represented by  $g(t)$ , where  $g_{\max}$  indicates the peak conductance measured in NanoSiemens (nS). The rise and decay of the synaptic conductance are characterized by the time constants  $\tau_1$  and  $\tau_2$ , respectively, both of which are measured in milliseconds (ms). Here,  $t$  stands for the time elapsed following the arrival of the presynaptic spike. This model effectively describes the dynamic behavior of synaptic conductance, which initially rises during the onset phase and subsequently undergoes a more prolonged decrease, a pattern common to both excitatory and inhibitory postsynaptic potentials (EPSPs and IPSPs). The variation in the time constants  $\tau_1$  and  $\tau_2$  facilitates the adjustment of the synaptic response's time profile, with  $\tau_1$  influencing the speed of onset and  $\tau_2$  affecting the length of the conductance alteration. For the parameters used, see table 2.1 and 2.2.

**Table 2.1:** Compartment dependent parameters used in the formulations of the three neuronal cell types according to equation 2.4. See appendix A for the full equations. The ionic conductances are in mS/cm<sup>2</sup>.

	$g_h$	$g_A$	$g_{Na}$	$g_K$	$V_{50}$	$b$	$c$	$d$	$e$	$f$
Bdend	0.1	48	32	10	-82	1	4	1.5	11	0.825
Soma	0.1	48	32	10	-82	0.8	4	1.5	11	0.825
Adend1	0.2	72	32	10	-82	0.5	4	1.5	11	0.825
Adend2	0.4	120	32	10	-90	0.5	2	1.8	-1	0.7
Adend3	0.7	200	32	10	-90	0.5	2	1.8	-1	0.7

The synaptic connections between neurons were implemented as follows:

**Table 2.2:** Synaptic Parameters for the Connectivity Between Neurons in the Model: Pre- and postsynaptic receptor types are given for each cell type. The time constants  $\tau_1$  and  $\tau_2$  are in milliseconds.  $\tau_1$  is the rise time constant, the time it takes for synaptic conductance to increase from baseline to peak.  $\tau_2$  is the decay time constant, the time it takes for the conductance to decrease from peak to baseline. The conductance indicates the strength of the synaptic connection and its ability to conduct ionic current across the postsynaptic membrane. This influences the extent to which the synaptic input can depolarize the postsynaptic neuron and is in nanoSiemens (nS).

Presynaptic	Postsynaptic	Receptor	$\tau_1$ (ms)	$\tau_2$ (ms)	Conductance (nS)
Pyramidal	Pyramidal	AMPA	0.05	5.3	0.02
Pyramidal	Pyramidal	NMDA	15	150	0.004
Pyramidal	Basket	AMPA	0.05	5.3	0.36
Pyramidal	Basket	NMDA	15	150	1.38
Pyramidal	OLM	AMPA	0.05	5.3	0.36
Pyramidal	OLM	NMDA	15	150	0.72
Basket	Pyramidal	GABA-A	0.07	9.1	0.72
Basket	Basket	GABA-A	0.07	9.1	4.5
Basket	OLM	GABA-A	0.07	9.1	0.0288
OLM	Pyramidal	GABA-A	0.2	20	72
MS	Basket	GABA-A	20	40	1.6
MS	OLM	GABA-A	20	40	1.6

For the full overview of synaptic parameters, see appendix B.

## 2.4 Model implementation: stimulation and noise

The model was activated by external inputs originating from the entorhinal cortex, which were then transmitted to the pyramidal cells. Background random excitatory and inhibitory inputs were received by the OLM, basket cells, and the soma of the pyramidal cells via their AMPA, NMDA, and GABA-A receptors as shown in table 2.2. The mechanism by which noise was applied to the model was defined via NEURON simulator's *NetStim* object. This object type generated spike train according to a set of parameters such as stimulus interval, noise variability (Poisson-like), weight, target, start and delay times. These parameters can be viewed in Appendix A.

Similarly, the distal dendritic compartments of the pyramidal cells also received comparable inputs through the same types of receptors. Connections such as OLM to pyramidal cell, basket to pyramidal cell, basket-basket recurrent connections, and medial septum to OLM and basket cell connections were mediated through GABA-A receptors. Additionally, the medial septum provided inhibitory inputs to the basket and OLM cells at intervals of 150 ms.

## 2.5 Simulations

For the simulations, the model was implemented in NEURON version 7.6.3. The simulations were run on a Linux GNOME (v22.04) desktop computer with 2 Xeon CPU E5-2699 v3 CPUs with 32 physical cores @ 2.3GHz for multi-threading, a Nvidia GTX 4060 graphics card, and 256 GB of RAM. Trials were run for 5000 ms with a time integration step of 0.1 ms resulting in 50.000 simulation steps per trial dataset. Random seeds were used to generate the external noise, connections and cells for each trial and remained constant between trials and between experiments. The number of trials varies between experiments and are specified in their respective sub-sections that follow. In the network, the individual cells were assigned a global identifier (GID) to which all the data was associated in the same ascending order for each trial. The first 800 cells were always pyramidal cells, the next 200 were basket cells and the last 200 were OLM cells. For each trial, the individual cell spike times were saved for the entire duration of the simulation. Pyramidal cell membrane soma voltage data was saved per cell in order to calculate the LFP signal (necessary for theta-gamma calculations).

### 2.5.1 Baseline activity

In order to obtain baseline activity in the network as shown in figure 2.1, current injections were added (**Pyramidal cells:** 50 pA; **OLM cells:** -25 pA). At Baseline, the network generates theta-modulated gamma oscillations activity. This activity was measured from the Local Field potential (LFP) in the network. The LFP was simulated by a sum difference between membrane potential of the distal apical and basal dendritic compartment over all pyramidal cells. As discussed in the cell parameters section, all cells contained leak current, transient sodium current  $I_{Na}$ , and delayed rectifier current  $I_{K,dr}$  to allow for action potential generation. On average, the firing rates were  $2.36 \pm 0.024$  Hz for pyramidal cells,  $16.05 \pm 0.15$  Hz for

basket cells and  $0.96 \pm 0.027$  Hz for O-LM interneurons at baseline in the original (Sanjay et al., 2015). However, it should be noted that our custom implementation of the same model had a slightly lowered baseline (see the results section). The reason for this discrepancy is unknown and is a potential source of error in the results. 50 trials total were done for the baseline activity and averaged.

### 2.5.2 Model validation

In order to test the implementation of the model, results from the article were replicated, namely figures 6A, B and C from Sanjay et al. (2015). In this replicated experiment the OLM to pyramidal cells connection weight was reduced in decrements of 0.1x times the baseline from 1.0 to 0.0. In addition to reduced connection strength, the external noise fed into the pyramidal cells was increased in increments of 0.1X times the baseline from 1.0 to 2.0. By reducing the connectivity from OLM to pyramidal cells, dendritic inhibition was impaired and potential epileptiform activity was induced.

The original results on which the validation experiment focussed on, were the following three aspects: changes in firing rates per population, the changes in dominant theta and gamma frequencies, and finally the changes in the power of the theta and gamma oscillations (see figure: 2.2). The numerical results from are in the following table:

**Table 2.3:** Overview of Original Network Simulation Settings and Outcomes. This table contains all the original results of figure 6 from the Sanjay et al. (2015) article. Variations in the firing rates of single cells, alongside theta and gamma oscillations within the local field potential, as well as the alterations in their intensity upon the decrease of dendritic inhibition and the concurrent enhancement of external stimuli to the pyramidal neurons.

OLM-Pyr Wt	External Wt	Pyr (Hz) + Std	BWB (Hz) + Std	OLM (Hz) + Std	Theta Freq (Hz)	Theta power (mV <sup>2</sup> Hz <sup>-1</sup> )	Gamma Freq (Hz)	Gamma power (mV <sup>2</sup> Hz <sup>-1</sup> )
1x	1x	$2.36 \pm 0.024$	$16.05 \pm 0.15$	$0.96 \pm 0.027$	6.7	5.35	33.2	2.55
0.8x	1.2x	$2.66 \pm 0.029$	$19.88 \pm 0.11$	$1.11 \pm 0.03$	6.7	5.4	32.5	2.4
0.6x	1.4x	$2.9 \pm 0.03$	$21.04 \pm 0.15$	$1.42 \pm 0.03$	6.7	4.1	32.4	5.3
0.4x	1.6x	$3.19 \pm 0.033$	$22.15 \pm 0.15$	$1.93 \pm 0.03$	6.7	2.2	31.7	3.6
0.2x	1.8x	$3.67 \pm 0.036$	$23.97 \pm 0.15$	$2.64 \pm 0.036$	6.7	2	32.7	6.5
0.1x	1.9x	$4.24 \pm 0.038$	$26.98 \pm 0.15$	$3.35 \pm 0.034$	6.7	1.16	33.9	11.4
0.05x	1.95x	$4.5 \pm 0.04$	$21.68 \pm 0.25$	$3.69 \pm 0.033$	6.7	0.65	37.8	1.55
0x	2x	$6.14 \pm 0.054$	$24.26 \pm 0.44$	$4.98 \pm 0.035$	0	0	38.8	1.32

### 2.5.3 Sodium and potassium variants

In this experiment, the sodium and potassium conductances of the all cell types cells were changed from 0.5x to 1.5x times the baseline in increments of 0.1. The changes were induced in separate experiments for each of the three cell types, so 6 experiments in total were conducted: 3 for sodium and 3 for potassium. These induced changes were done in order to investigate the effect of the conductances on the network activity and the influence of individual cell types on the same metrics as in the model validation experiment. 20 trials each were done per condition (6 total conditions) and the results were averaged.

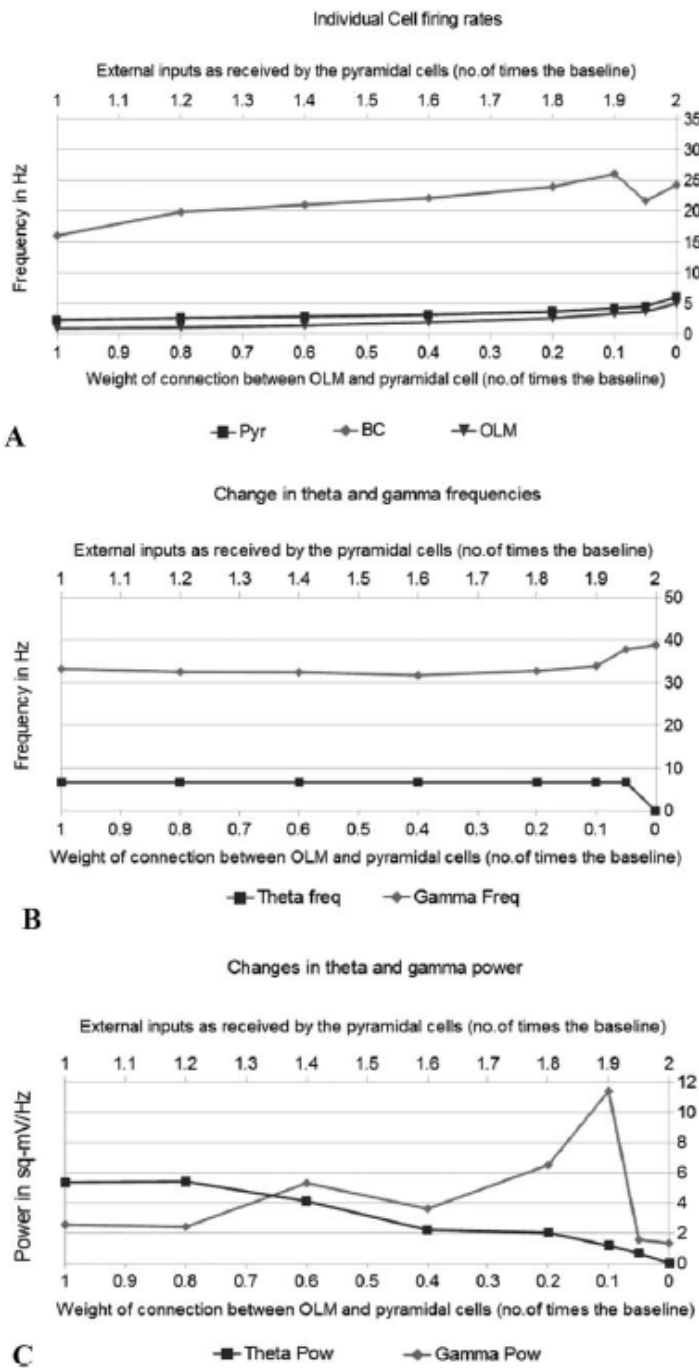


**Figure 2.2:** Sanjay article results: Figure 6

The validation experiment was conducted to replicate the results of Sanjay et al. (2015) in order to verify the implementation of the model. The experiment involved reducing the connection strength from OLM to pyramidal cells and increasing the external noise fed into the pyramidal cells. The firing rates per population (A), dominant frequencies in the theta-gamma bands (B) and their respective average power (C) was investigated. The results were compared to the original article to verify the implementation of the model (see Results section).

## Visualization of Neuronal Activity Variants

This section outlines the analytical approach adopted for visualizing the neuronal activity within our network model under different experimental conditions. Specifically, we focused on plotting the firing rates, theta-gamma frequencies, and theta-gamma power across all neuronal populations (pyramidal, basket, and OLM cells) for variants induced by alterations in sodium and potassium conductance levels.

### Firing Rate Analysis

We initiated our analysis by examining the firing rates across different cell populations. A comparative visualization was generated to juxtapose the mean firing rates under sodium and potassium variant conditions, utilizing a grid layout for a side-by-side comparison. Each plot incorporated error bars to represent the standard error of the mean (SEM), thereby conveying the variability inherent in our simulation trials. Cell populations were differentiated by distinct markers and colors to facilitate clear distinction between pyramidal, basket, and OLM cells across varying conditions.

### Theta-Gamma Frequency Analysis

Subsequent to firing rate analysis, we delved into the investigation of theta and gamma frequency bands. For each variant type (sodium and potassium), theta and gamma frequencies were plotted on a  $2 \times 2$  grid, delineating the mean frequency values extracted from the simulation data. This approach allowed for an intuitive understanding of the oscillatory dynamics prevalent in the network under different ionic conductance conditions, highlighting potential shifts in theta-gamma coupling associated with epileptiform activities.

### Theta-Gamma Power Analysis

In addition to the frequency analysis, the power of theta and gamma oscillations were quantified. This step aimed to investigate the intensity of oscillatory activity within these critical frequency bands. Similar to our frequency analysis, a  $2 \times 2$  grid layout facilitated the comparison of theta and gamma power across sodium and potassium variants. This visual representation served to elucidate variations in oscillatory power, potentially correlating with changes in network excitability and synchronization under altered ionic conditions.

### Power Spectral Density (PSD) Calculation

The aforementioned theta-gamma analyses used the `calc_psd` function to compute the power spectral density (PSD) of an LFP signal, focusing on theta (3–12 Hz) and gamma (30–80 Hz) frequencies. Initial signal processing includes discarding the first millisecond to avoid transient effects and down-sampling according to a predefined maximum frequency ( $f_{max}$ ). The PSD calculation uses a Fast Fourier Transform (FFT) approach, adjusting for the signal mean. For both theta and gamma ranges, the function identifies relevant frequencies, calculates mean power by averaging power values within these ranges, and identifies the dominant frequency

by locating the frequency with the maximum power value. This analysis facilitated the quantification of signal power and rhythmic activity within specific frequency bands, essential for understanding neural dynamics in these ranges.

#### 2.5.4 External noise variants

In this experiment, the external noise fed into the pyramidal cells was set a new baseline for the 1.0x condition, which was 20 times that of the original Sanjay et al. (2015) model. Reduced OLM to pyr connections were kept at 10% of the original baseline. This was done because in the original article, epileptic activity was induced by feeding in 20 times more external noise at reduced dendritic inhibition.

This condition was tested as a special condition in figure 7 of the article, and was expanded upon because of the occurrence of a depolarization block in the basket cell spike activity. This depolarization block occurrence was assumed to be the epileptic state in which the network is found at such conditions. This new baseline was changed times a range of pyramidal noise factors of the following values: 0.65, 0.70, 0.75, 0.80, 0.85, 0.90, 0.95, 1.00, 1.10, 1.20, and 1.30. In addition to the range of noise factors, pyramidal conductances  $g_{Na}$  and  $g_K$  were modified over a range of 0.5x to 1.5x times the baseline in increments of 0.1. 15 trials were done per noise condition and the results were averaged.

#### Detection of epileptiform activity (Experiments: External Noise and Recurrent Connection strength variants)

The detection of epileptic activity depends on the spiking activity of the basket cells, which according to results of figure 7 from the Sanjay et al. (2015) article occurs in the presence of great external drive from the pyramidal cells of at least 20 times the baseline and with reduced dendritic inhibition by the OLM cells. Detection of a depolarization block in the basket cells was done by calculating the convoluted fire rates of the basket cell population.

The systematic approach to analyzing basket cell firing rates through convolution with a Gaussian window was as follows:

- **Extracting Spike Times:** The `get_spike_times_for_basket_cells` function is used for iterating over a range of GIDs. This process collects spike times from all basket cells and concatenates them, constructing a continuous signal of neural activity.
- **Creating Time Series:** Spike times are converted into a binary series using `create_time_series`. Each neural firing event is denoted by a '1' in a zero-initialized array at the corresponding time index.
- **Applying Gaussian Convolution:** The `apply_gaussian_convolution` function smooths the time series. It convolves the series with a Gaussian window, normalized to sum to one, yielding a signal that mirrors the firing rates over time.
- **Summing Convolved Signals:** Collective firing behavior is analyzed by `get_convolved_signal_per_neuron`. It applies Gaussian convolution to individual neuron time series and sums them, forming an aggregated firing rate signal.

- **Detecting Depolarization Blocks:** The `detect_depolarization_blocks` function identifies reduced activity periods by analyzing the convolved signal for intervals that remain below a set threshold for a specified minimum duration.

*This method for detecting depolarization blocks in the basket cell population and convolution of spike activities was also used for the recurrent connection strength variants experiment below. See the example in figure 2.3.*

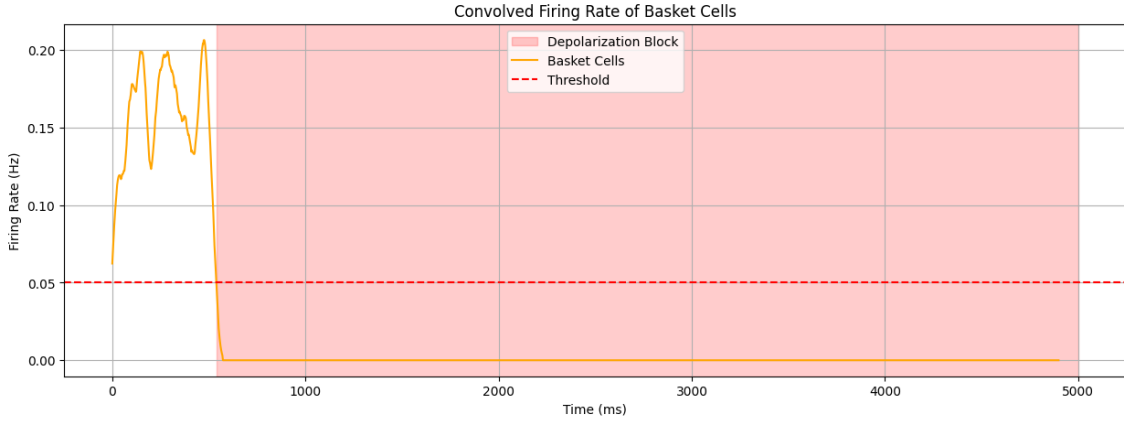


**Figure 2.3:** Depolarization block in basket cells. Example of a single trial where a depolarization block is found in the convoluted spike activity signal as a flat-line at 0 Hz. The firing rate is in Hz (y-axis) and the signal is calculated over the entire duration of the trial (5000 ms). Note that the signal has to pass the threshold for an extended period of 100 ms to be considered a DPB. In addition, the first 50 ms are excluded from detection to avoid false positives. This detection method was done for each individual trial.

## Analysis of External Noise Variants

This section elaborates on the methodological approach undertaken to assess the impact of varying levels of external noise on pyramidal cells, with the aim of understanding its influence on depolarization block occurrences within the network. The experiment's premise was based on the hypothesis that adjusting the external noise could modulate the epileptic state, characterized by depolarization blocks, within the neural network.

The analysis was structured as follows:

1. **Event Detection and Quantification:** For each variant of external noise levels, depolarization events were systematically identified. These results were quantified per trial. This process involved the enumeration of depolarization events, accumulation of their start and end times, and the computation of the overall duration of these events within each trial.
2. **Statistical Analysis:** Subsequent to the detection of depolarization events, the analysis proceeded with the calculation of average event duration and the computation of the percentage of trials exhibiting depolarization blocks. Furthermore, the mean delay and standard deviation for the onset of depolarization events were determined to gauge the temporal dynamics of the network's response to varying noise levels.
3. **Data Visualization:** To concisely present the findings, the analysis results were visualized through matrix plots. These plots delineated the relationship between pyramidal conductances ( $g_{Na}$  and  $g_K$ ) and the observed network behavior under different external noise conditions. The visualizations highlighted the proportion of trials with depolarization blocks and detailed the temporal onset characteristics of these events, facilitating an intuitive understanding of the network's epileptic susceptibility.

The investigative focus on external noise variants sought to delineate the conditions under which the network transitions into an epileptic state, as indicated by the presence of depolarization blocks. Through a comprehensive compilation of quantitative and visual analyses, this study aimed to unravel the complexities of neural dynamics in response to altered external stimulation, thereby contributing to a deeper insight into potential mechanisms for modulating epileptiform activities.

### 2.5.5 External noise: Burst analysis

Further analysis was conducted to investigate the burst dynamics of pyramidal and basket cell activity based on the observations done in the initial increased noise experiment. This experiment involved looking at the temporal shift in detected bursts surrounding the onset of a depolarization block event in the basket cell population.

#### Detection of Epileptiform Activity and Burst Analysis

This experiment employed a novel method for the detection of epileptiform activity, leveraging convolved spike activities and burst detection within neural populations. The approach was predicated on analyzing the temporal dynamics of neuronal firing rates, specifically focusing on the basket and pyramidal cell populations. A critical aspect of this analysis was the identification and analysis of bursts in relation to the onset of depolarization blocks (DPBs), offering insights into the neural dynamics associated with epileptiform activity.

The unified methodology proceeded as follows:

- **Identification of Depolarization Block Onset:** A custom python function `find_depolarization_block` was employed to scan the simulation data for periods devoid of spiking activity within a specified window across basket cell populations. This step was crucial in pinpointing the initial point of a depolarization block, thus serving as a reference for the subsequent analysis.
- **Preparation and Convolution of Spike Activities:** Spike times were aggregated and subjected to a Gaussian filter, smoothing the data to represent neural firing rates over time effectively. This step facilitated the identification of significant patterns in relation to the DPB onset.
- **Burst Detection and Temporal Analysis:** The convolved spike activities were analyzed using a burst detection algorithm, identifying significant increases in activity as bursts. These were classified based on their occurrence relative to the DPB onset—focusing on the last burst before, the second-last burst before, and the first burst after the onset. This classification shed light on the changes in neural dynamics preceding and following a depolarization block.
- **Analytical Assessment and Summarization of Findings:** Start and end times were determined for detected bursts, as well as peak activity levels. This comprehensive analysis of convolved spike activities and burst dynamics provided a detailed view of the neural mechanisms during critical phases of epileptiform activity.

The experiment utilized a 100 ms window and a 0.1 ms time step throughout the 5000 ms simulation duration, resulting in 50,000 indices for spike detection. The absence of basket cell firing within this window indicated a DPB, which was critical for burst detection. This methodology offered a nuanced understanding of epileptiform dynamics, highlighting the transitions of neural populations into and out of depolarization blocks which are indicative of epileptic activity in the network. Note that in the burst analysis the 1D-Gaussian convolution was performed on a histogram of the spike times of cells. Whereas in the previous convolution for the matrices, the convolutions were performed using a binary time series of the spike times.

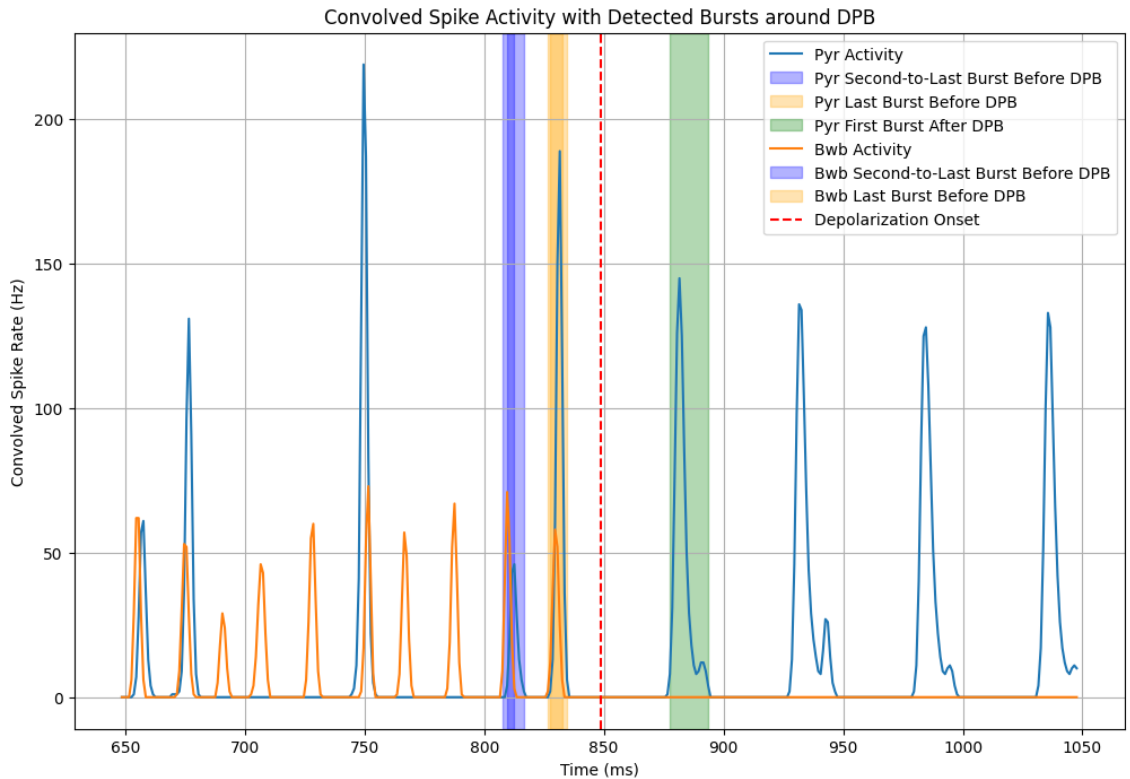


**Figure 2.4:** Burst detection example. Example of a single trial where bursts in the neural populations are detected near the onset of a DPB using convoluted spike activity signals. The firing rate is in Hz (y-axis) and the signal is calculated over the entire duration of the trial (5000 ms). The onset of a depolarization block in basket cells is indicated by a red dashed vertical line. The last and second to last bursts before, and the first burst after the DPB were detected and used for analysis. Note that the signal has to pass the threshold for an extended period of 100 ms to be considered a DPB. In addition, the first 50 ms are excluded from detection to avoid false positives. This detection method was done for each individual trial.

## 2.5.6 Recurrent connection strength variants

This section describes the methodology employed to analyze the effects of varying recurrent connection strengths between basket cells on the incidence and characteristics of depolarization blocks within the network. This analysis aimed to explore the potential of modulating soma inhibition strength to mitigate epileptic activity and restore baseline network dynamics.

The experiment adjusted the recurrent connection strength across a range of multipliers (1.00, 1.05, 1.10, 1.15, and 1.20 times the baseline), concurrently with modifications to  $g_{Na}$  and  $g_K$  within a plus or minus 25% range of the baseline. The connection weight from OLM cells to pyramidal cells was fixed at 10%, facilitating the induction of depolarization blocks under a 20x external noise condition on pyramidal cells. A total of 15 trials were conducted for each condition, and the results were averaged for analysis.

### Analysis of Recurrent Connection Strength Variants

The analysis procedure was as follows:

1. **Event Detection and Aggregation:** The analysis began by identifying depolarization events across trials for each variant of the recurrent connection strength. This involved counting the number of depolarization events, their start and end times, and the total duration of depolarization within each trial. Trials devoid of depolarization events were separately tallied.
2. **Statistical Computation:** For trials exhibiting depolarization events, the average duration of these events was calculated. Additionally, the percentage of trials manifesting depolarization events and the statistical measures (mean and standard deviation) concerning the onset times of these events were determined.
3. **Matrix Visualization:** The analyzed data were visualized using matrix plots to illustrate the relationship between the recurrent connection strength variants and the properties of depolarization events under different  $g_{Na}$  and  $g_K$  conditions. These plots highlighted the percentage of trials with depolarization blocks and the count of depolarization events, offering insights into the efficacy of soma inhibition strength adjustments in modulating epileptic activity.

This analytical approach facilitated a comprehensive examination of the impact of modifying recurrent connection strengths among basket cells on the network's susceptibility to epileptic disruptions. Through statistical and visual analyses, the dynamics governing epileptiform activity and the potential for intervention was investigated through targeted manipulation of inhibition mechanisms within the neural circuitry.

For detecting depolarization blocks in the basket cell population, the methodology was as follows:

- Establishing a signal threshold indicating a depolarization block.
- Excluding initial transient analysis to prevent false positives.

- Identifying threshold crossings that mark the start and end of depolarization blocks.
- Applying a minimum duration filter to these blocks.
- Summarizing and reporting the total duration of all valid depolarization blocks in the trial.

A check was performed if the convoluted signal remained beneath a fixed threshold of 0.001 for at least 100 ms. This threshold was defined non-zero, yet tiny as in the depolarization block there are no firing neurons in the basket population. The first 50 ms of the signal were excluded to avoid false positives. If the signal remained beneath the threshold for at least 100 ms, the condition was considered to be in a depolarization block state. This was done for each trial individually. An example of this can be seen in figure 2.3.

# 3 Results

## 3.1 Results of the Baseline activity

In the initial experiment, the baseline activity of the CA3 network was observed from the *original model* by Sanjay et al. (2015). The network was simulated for 5000 ms and showed synchronous activity throughout all three populations (pyr, BC and OLM). Basket cells showed a higher firing rate compared to the pyramidal cells and O-LM cells. The basket cells also swapped between states of synchrony and asynchrony which was not observed in the other two populations. The O-LM cells showed the lowest firing rate compared to the pyramidal cells and basket cells. The baseline activity of the CA3 network is shown in figure 3.1.

The average firing rates of the populations were  $2.36 \pm 0.024$  Hz for pyramidal cells,  $16.05 \pm 0.15$  Hz for basket cells, and  $0.96 \pm 0.027$  Hz for O-LM interneurons, similar to observed results from Neymotin et al. (2011) which used the same model on which the Sanjay model is based upon.

Just as reported in the original article, the network produces theta-modulated gamma oscillations within the local field potential (LFP). These oscillations were influenced by signals from the Medial Septum (MS). The gamma oscillations emerged from the inhibitory connections between basket cells that inhibit somas of pyramidal and O-LM cells, as well as interactions among basket cells themselves. Conversely, theta oscillations were the result of interactions between pyramidal cells and O-LM cells that inhibit dendrites. The network achieved a consistent theta frequency of 6.7 Hz due to periodic inputs from the MS to both O-LM and basket cells every 150 ms. The frequency of the gamma component within the LFP was approximately 33 Hz. Despite receiving similar MS inputs as O-LM cells, the impact on basket cells was significantly reduced because of their mutual interactions and the enhanced influence from pyramidal cells.

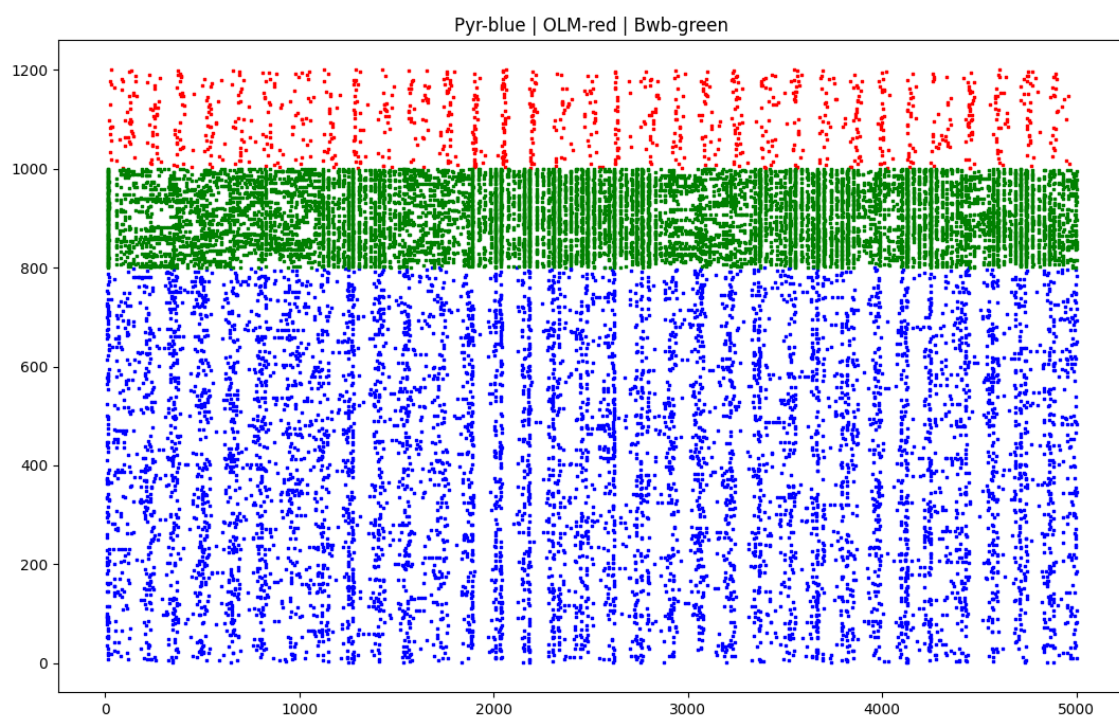


**Figure 3.1:** Baseline activity of the CA3 network.

The above figure shows the baseline activity of the CA3 network. The network was simulated for 5000 ms. The spike activity in time of the Pyr cells, BC cells, and OLM cells are shown based on the Neuron ID. ID 0–799 = Pyramidal (blue), 800–999 = BC (green), 1000–1200 = OLM (red). The x-axis represents the time in ms and the y-axis represents the neuron ID.

## 3.2 Results of the Model validation

To test whether our implementation of the CA3 network was able to replicate more elaborate results, results from figure 6 of the original Sanjay et al. (2015) article were replicated in figure 3.4, 3.5 and 3.6.

Like in the original experiment, O-LM-pyramidal connectivity was decreased in decrements of 0.1 and reduced dendritic inhibition. Simultaneously, external noise fed to pyramidal cells via AMPA and NMDA at the synaptic level was increased in increments of 0.1. When O-LM-pyramidal connectivity was decreased to a range of 20–10 %, desynchronization was observed among basket cells (figure 3.2). Complete desynchronization was observed when the O-LM-pyramidal connectivity was reduced to 0 % (figure 3.3). Pyramidal to O-LM connectivity was unchanged, thus these cells showed sustained synchronous activity.

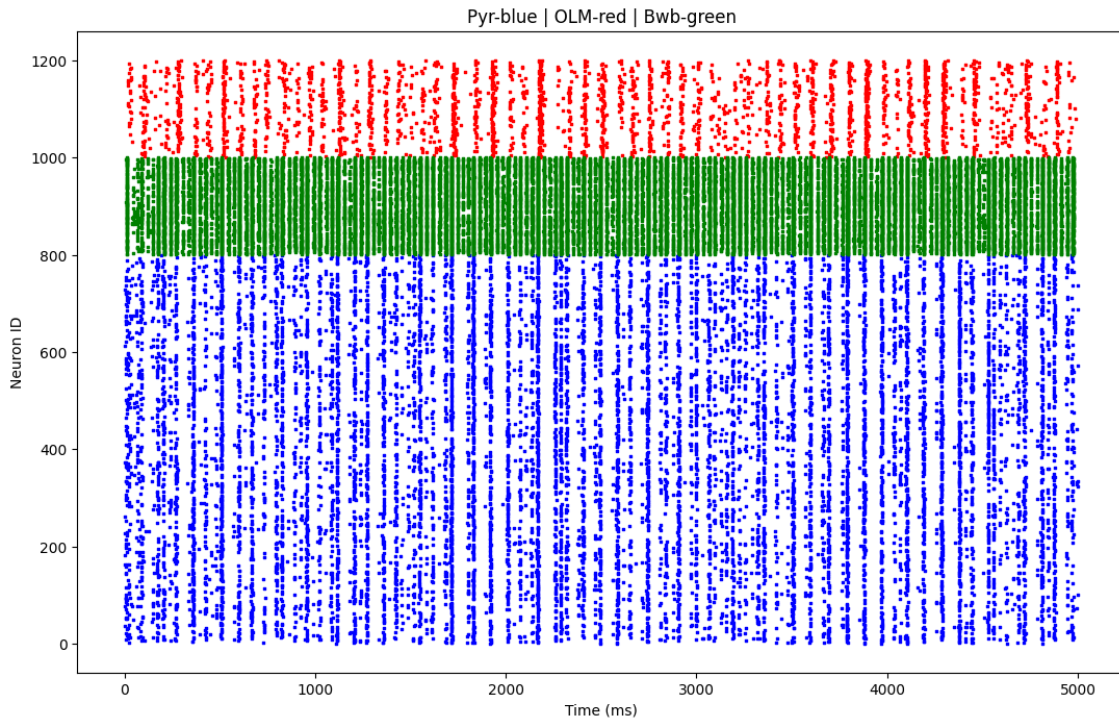


**Figure 3.2:** Scatter plot of the network activity at 20 % OLM-Pyr connection

The above figure shows the network activity at 20 % OLM-Pyr connection with significant asynchrony amongst the basket cells. The network was simulated for 5000 ms. The scatter plot shows the spike activity of the Pyr cells (blue), BC cells (green), and OLM cells (red). The x-axis represents the time in ms and the y-axis represents the neuron ID.

The results show that the model was able to replicate the results of the original article with slightly lower firing rates, theta-gamma frequencies and power, which can be seen in table 3.1. The original article results are visible in the methods section in table 2.3 for comparison.

For the firing rates in figure 3.4, there was a notable increase in the firing rates of all neuron types as dendritic inhibition was decreased while external noise was simultaneously increased. The individual cell firing frequencies showed a near linear increase throughout in both pyramidal and O-LM cells, being most pronounced

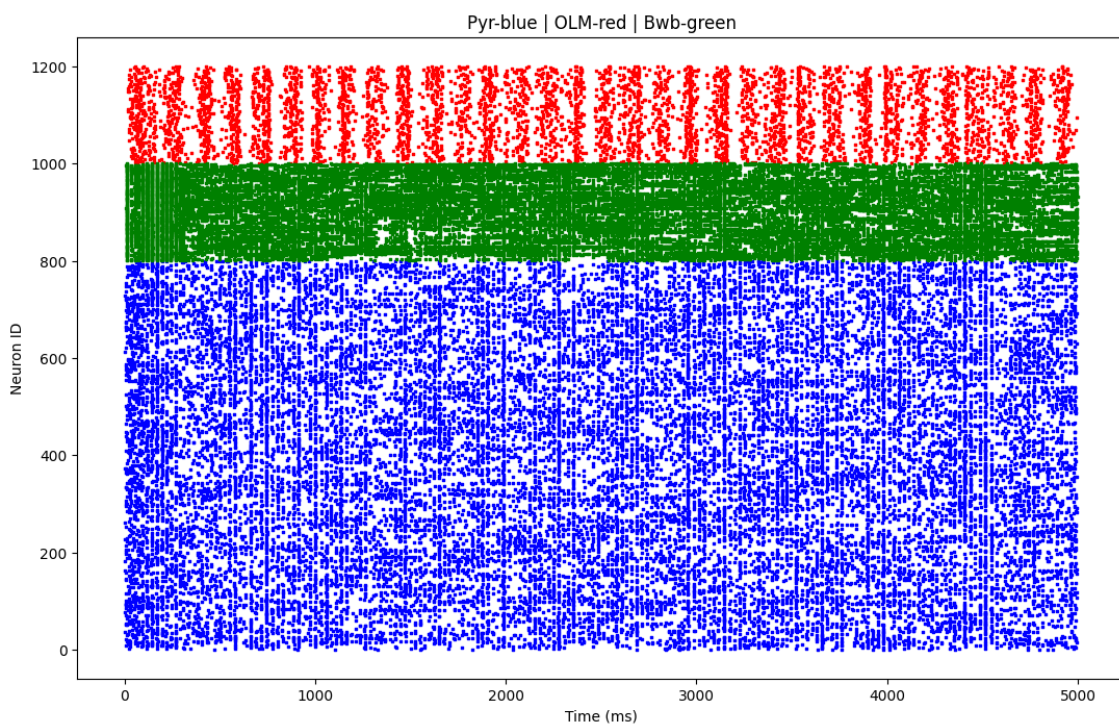


**Figure 3.3:** Scatter plot of the network activity at 0 % OLM-Pyr connection  
The above figure shows the network activity at 0 % OLM-Pyr connection with complete asynchrony amongst the basket cells. The network was simulated for 5000 ms. The scatter plot shows the spike activity of the Pyr cells (blue), BC cells (green), and OLM cells (red). The x-axis represents the time in ms and the y-axis represents the neuron ID.

in the basket cell population. The basket cell population also showed the most variance in the standard deviation at the most extreme condition from the baseline (0.0x OLM-Pyr weight and 2.0x external weight).

The dominant frequencies in the network activity, as shown in figure 3.5, showed that the theta frequency remained constant, while the gamma frequency only increased as dendritic inhibition was severely decreased and external noise increased. The theta frequency remained constant at 6.2 Hz, slightly lower than the original model's 6.7 Hz, due to the strong pacing from the MS at this frequency.

The power of the theta and gamma oscillations in the network, as shown in figure 3.6, showed that the power of theta oscillations decreased, while the gamma power increased as dendritic inhibition was reduced. This shift in power distribution reflects changes in the balance of network excitability and inhibition, potentially leading to epileptic activity. The theta power reduced to  $5.35 \text{ mV}^2 \text{ Hz}^{-1}$  to  $0 \text{ mV}^2 \text{ Hz}^{-1}$ . The gamma power increased significantly from at 20 to 10 % O-LM-pyramidal connection. The gamma power increased from  $0.93 \text{ mV}^2 \text{ Hz}^{-1}$  at baseline to  $5.82 \text{ mV}^2 \text{ Hz}^{-1}$  before dropping down to  $1.87 \text{ mV}^2 \text{ Hz}^{-1}$  in the last condition. The gamma power was mostly due to basket cell activity, which were much more tightly synchronized than the other cell types.

The trends in the original figures were similar in figure 2.2 to the ones of this section. Therefore, it was assumed that the model was correctly implemented and the results were valid.

**Table 3.1:** Overview of Model Validation Network Simulation Settings and Outcomes. Variations in the firing rates of cell populations, alongside theta and gamma oscillations within the local field potential, as well as the alterations in their intensity upon the decrease of dendritic inhibition and the concurrent enhancement of external stimuli to the pyramidal neurons.

OLM-Pyr Wt	External Wt	Pyr (Hz) + Std	BWB (Hz) + Std	OLM (Hz) + Std	Theta Freq (Hz)	Theta power (mV <sup>2</sup> Hz <sup>-1</sup> )	Gamma Freq (Hz)	Gamma power (mV <sup>2</sup> Hz <sup>-1</sup> )
1.0X	1.0X	$1.83 \pm 0.58$	$9.21 \pm 2.20$	$1.08 \pm 0.38$	6.2	1.67	32.8	0.93
0.9X	1.1X	$2.00 \pm 0.64$	$10.67 \pm 2.31$	$1.15 \pm 0.36$	6.2	2.08	34.4	1.36
0.8X	1.2X	$2.00 \pm 0.71$	$11.54 \pm 2.72$	$1.22 \pm 0.39$	6.2	1.67	34.4	1.74
0.7X	1.3X	$2.14 \pm 0.74$	$13.24 \pm 2.36$	$1.29 \pm 0.42$	6.2	2.06	32.8	2.37
0.6X	1.4X	$2.33 \pm 0.79$	$15.04 \pm 2.35$	$1.44 \pm 0.45$	6.2	2.13	32.8	2.76
0.5X	1.5X	$2.41 \pm 0.80$	$16.44 \pm 2.31$	$1.53 \pm 0.45$	6.2	2.02	32.8	3.68
0.4X	1.6X	$2.57 \pm 0.79$	$17.88 \pm 2.12$	$1.76 \pm 0.45$	6.2	2.03	31.2	4.44
0.3X	1.7X	$2.74 \pm 0.86$	$19.04 \pm 2.38$	$2.10 \pm 0.49$	6.2	1.55	31.2	4.68
0.2X	1.8X	$2.97 \pm 0.88$	$20.61 \pm 2.14$	$2.44 \pm 0.48$	6.2	0.92	31.2	4.87
0.1X	1.9X	$3.59 \pm 0.99$	$20.98 \pm 2.62$	$3.31 \pm 0.50$	6.2	0.78	32.8	5.82
0.0X	2.0X	$5.50 \pm 1.52$	$21.46 \pm 7.93$	$4.90 \pm 0.52$	4.7	0.04	39.1	1.87

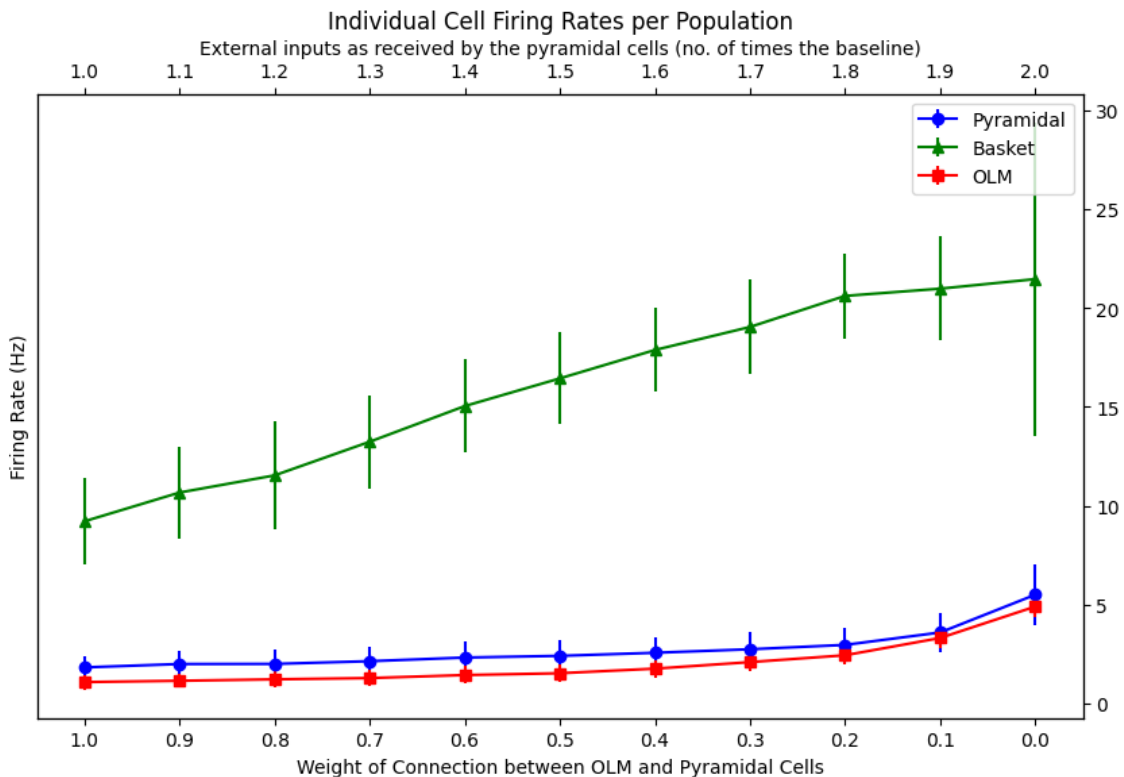


**Figure 3.4:** Validation of the firing rates.

The above figure shows the firing rates of the Pyr cells, BC cells, and O-LM cells when dendritic inhibition is decreased and external noise is increased. The firing rates were calculated from the spike activity of the cells in each population for the duration of the simulation (5000 ms). The double x-axis represents both decrement in the weight of dendritic inhibition on pyramidal cells by OLM interneurons, while simultaneously increasing external noise stimulation to pyramidal cells. External noise levels rise and inhibition decreases by increments of 0.1, each representing a 10% change relative to the baseline. The y-axis represents the firing rate in Hz. The firing rates are per cell type: Pyr (blue), Basket (green) and OLM (red). The error bars represent the standard deviation of the firing rates.

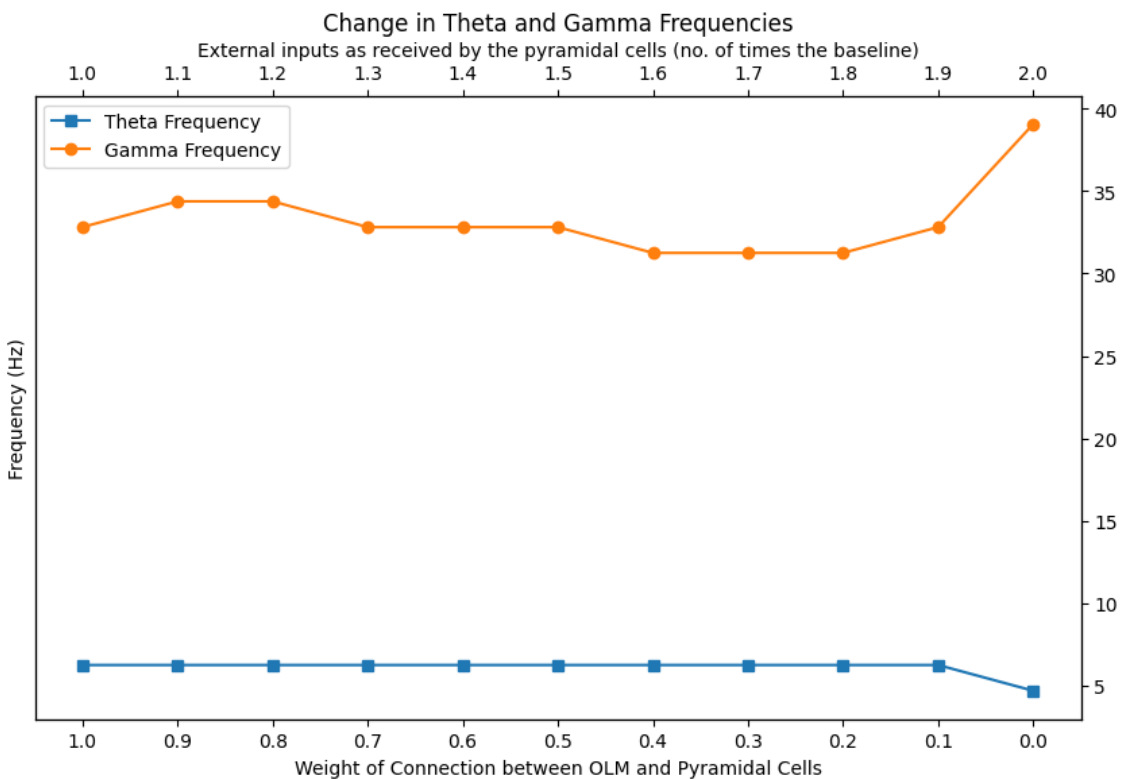


**Figure 3.5:** Validation of dominant frequencies.

The above figure shows the dominant theta-gamma frequencies in the network activity when dendritic inhibition is decreased and external noise is increased. The double x-axis represents both decrement in the weight of dendritic inhibition on pyramidal cells by O-LM interneurons, while simultaneously increasing external noise stimulation to pyramidal cells. External noise levels rise and inhibition decreases by increments of 0.1, each representing a 10% change relative to the baseline. The y-axis represents the dominant frequency in Hz for both theta (3–12 Hz, blue) and gamma (30–80 Hz, orange) oscillatory bands.

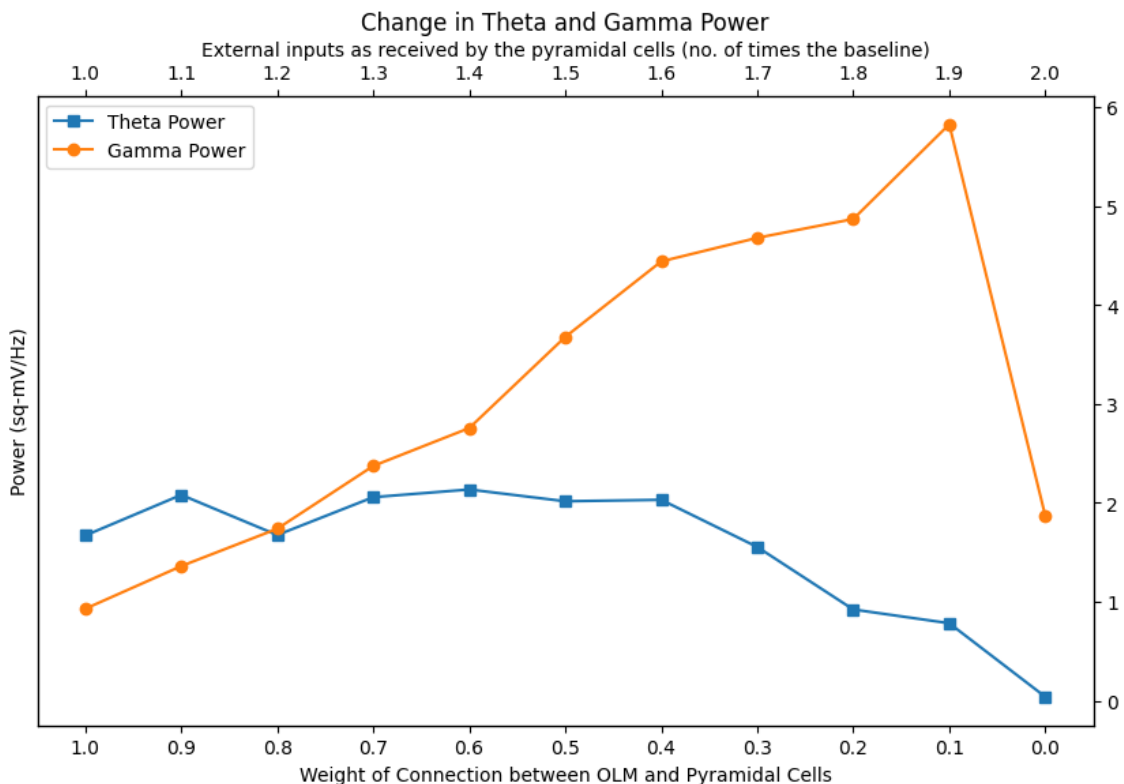


**Figure 3.6:** Validation of Theta-Gamma power.

The above figure shows the power of the theta and gamma oscillations in the network when dendritic inhibition is decreased and external noise is increased. The double x-axis represents both decrement in the weight of dendritic inhibition on pyramidal cells by O-LM interneurons, while simultaneously increasing external noise stimulation to pyramidal cells. External noise levels rise and inhibition decreases by increments of 0.1, each representing a 10% change relative to the baseline. The y-axis represents the theta and gamma power (blue and orange, respectively).

### 3.3 Results of the Sodium-Potassium variants

In this experiment, the sodium and potassium conductance of the pyramidal, basket, and O-LM cells were modified in increments of 0.1. This was done in a range of 0.5 to 1.5 times the baseline conductance. Similarly to the previous experiment, the network was simulated for 5000 ms and the firing rates, dominant frequencies, and power of the theta and gamma oscillations were calculated in figures 3.7, 3.8 and 3.9, respectively.

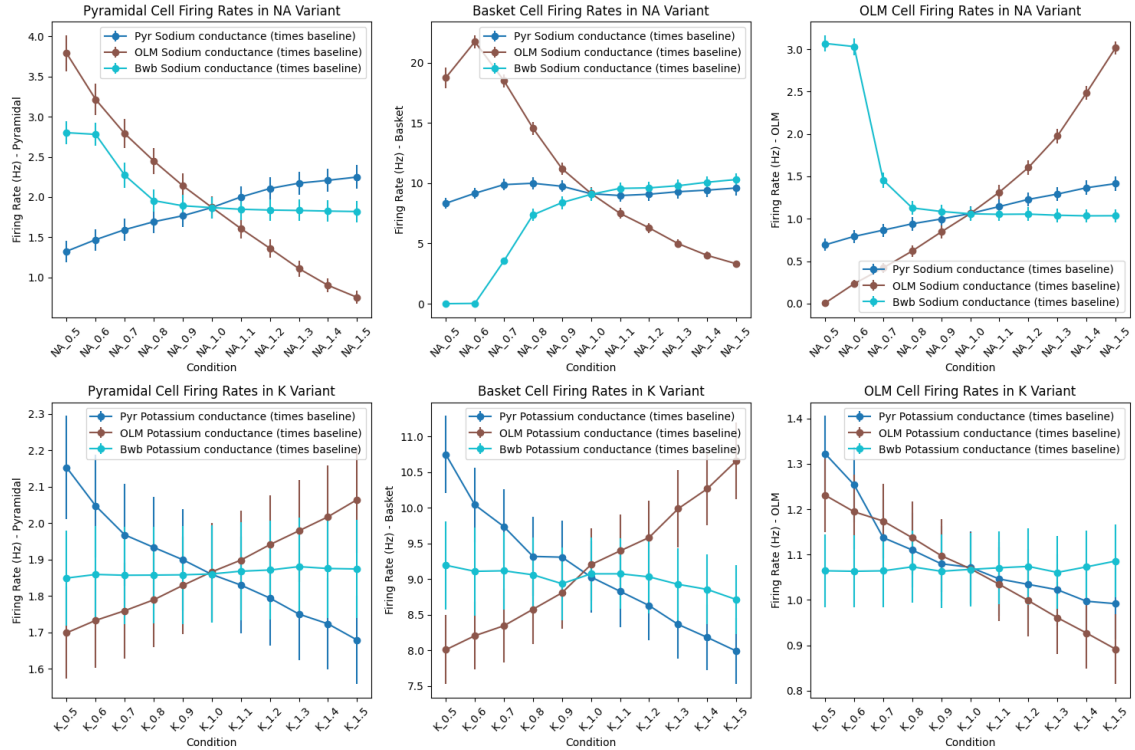


**Figure 3.7:** Sodium-Potassium variants: Firing rates per population.

The above figure shows the firing rates of the Pyr cells, BC cells, and O-LM cells for each modified cell type. Each of the three cell types either had modified sodium or potassium conductance. The firing rates were calculated from the spike activity of the cells in each population for the duration of the simulation (5000 ms). The x-axis represents the percentage amount of changed sodium or potassium conductance, times the baseline. The y-axis represents the firing rate in Hz. The firing rates are per cell type: Pyr (blue), Basket (cyan) and OLM (red). The error bars represent the standard error of the mean (SEM) of the firing rates per population.

#### 3.3.1 Firing rates: Pyramidal cells

In figure 3.7, the firing rates of pyramidal cells showed the largest change when the sodium conductance ( $g_{Na}$ ) of O-LM cells was modified. When the sodium conductance of O-LM cells (dendrite-inhibiting) was decreased, the firing rate of pyramidal cells increased, and vice versa. Sodium conductance of basket cells (soma-inhibiting) was also modified. Interestingly, the firing rate of pyramidal cells was unaffected

when  $g_{Na}$  was increased. However, when  $g_{Na}$  was decreased by more than 30 % the firing rate of pyramidal cells increased sharply. Lastly, increasing the  $g_{Na}$  in the pyramidal cells themselves led only to a marginal in- and decrease in firing rates.

Changing the potassium conductance ( $g_K$ ) had more profound effects on pyramidal firing rates. When the potassium conductance of O-LM cells was increased, the firing rate of pyramidal cells decreased, and vice versa. Changing  $g_K$  of basket cells had almost no effect on the firing rate of pyramidal cells. However, when the potassium conductance of pyramidal cells was modified, the effect of potassium on the pyramidal firing rates were almost the exact opposite of modified the O-LM cells.

### 3.3.2 Firing rates: Basket cells

Compared to pyramidal cell firing rates, the basket cell population has some significantly different trends in firing rates. When the  $g_{Na}$  of O-LM cells was modified, the firing rate of basket cells decreased, and vice versa. Interestingly, at -40 %  $g_{Na}$  of O-LM the firing rate peaks and then decreases sharply, instead of a linear decrease. Changing the  $g_{Na}$  of pyramidal cells had barely any effect on the firing rate of basket cells. Whereas changing the  $g_{Na}$  of basket cells themselves, led to a sharp decrease in firing rate at -30 %  $g_{Na}$  and a complete loss of firing at a -40 %  $g_{Na}$ . Generally, the firing rates were much higher and the effects on the firing rates were more pronounced compared to the pyramidal cells and O-LM cells (with the largest SEM).

Changing the  $g_K$  of basket cells had a similar effect to that of pyramidal population, albeit with larger in- and decreases in Hz. Just like the pyramidal firing rates, the basket firing rate increases when O-LM  $g_K$  is increased and vice versa. The firing rate of basket cells was unaffected when the  $g_K$  of basket cells was modified. Whereas increasing the  $g_K$  of pyramidal cells led to a decrease of basket cell firing rate and vice versa.

### 3.3.3 Firing rates: O-LM cells

The O-LM population showed the most unique variations in firing rates. When the  $g_{Na}$  of O-LM cells was modified, the firing rate of O-LM cells increased, and vice versa. However, when the  $g_{Na}$  of basket cells was decreased below -30 %, the firing rate of O-LM cells increased sharply to more than double the Hz. Pyramidal  $g_{Na}$  had a weak and linear effect on the O-LM firing rates, where increased  $g_{Na}$  led to increased firing rates and decreased  $g_{Na}$  led to decreased firing rates.

Changing the  $g_K$  of O-LM cells had an inverted effect on firing rates compared to  $g_{Na}$ . Modifications to basket cell  $g_K$ , again, had little to no effect on the firing rate of O-LM cells. However, when the  $g_K$  of pyramidal cells was modified, the effect on the O-LM firing rates was almost the same as the O-LM  $g_K$  modifications.

### 3.3.4 Dominant frequencies

In this experiment the dominant theta and gamma frequencies were identified from the local field potential (LFP) for the duration of the simulation (5000 ms) by performing a power spectrum density analysis. The dominant frequencies were calculated for each modified cell type and are shown in figure 3.8. The figure is split in both sodium and potassium conductance modifications for each cell type (pyramidal = blue, OLM = red, basket = cyan).

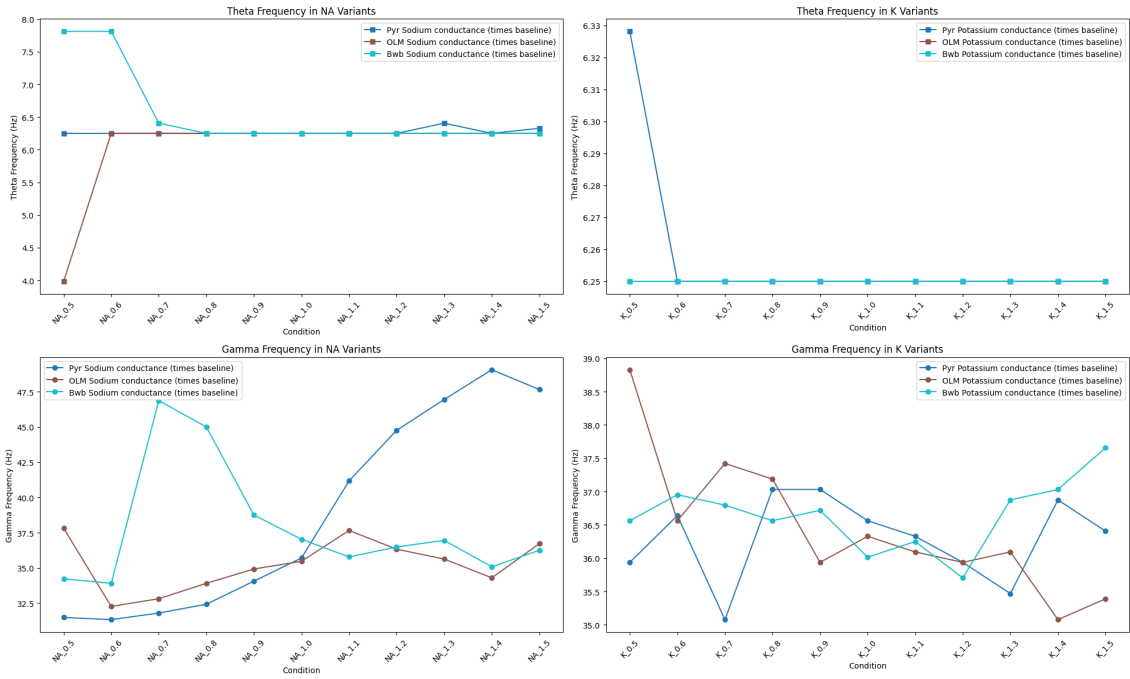


**Figure 3.8:** Sodium-Potassium variants: Dominant frequencies.

The above figure shows the dominant theta-gamma frequencies in the network activity for each modified cell type. Each of the three cell types either had modified sodium or potassium conductance (pyr = blue, OLM = red, basket = cyan). The dominant frequencies were calculated from the local field potential (LFP) for the duration of the simulation (5000 ms). The x-axis represents the percentage amount of changed sodium or potassium conductance, times the baseline. The y-axis represents the dominant frequency in Hz for both theta (3–12 Hz) and gamma (30–80 Hz) oscillatory bands.

### Theta frequency

For both sodium and potassium conductance modifications, the theta frequency was largely unaffected as it is generated by the strong pacemaker influence of the medial septum at the 6.2 Hz frequency. There were a couple of outliers in both conditions, in the -50 % conditions of O-LM and basket  $g_{Na}$ , is decreased and increased respectively (3.8, top left = sodium theta, right = potassium theta).

## Gamma frequency

Conversely, the gamma frequency was more affected by the sodium and potassium conductance modifications. In the modified pyramidal condition the gamma frequency increased sharply from -50 % to 50 %  $g_{Na}$  from 30.4 Hz to 48.8 Hz. O-LM modifications in comparison, had a less significant effect on the gamma frequency, with a slight increase from the baseline at 10 % increased  $g_{Na}$ . Basket cell modifications had the most significant effect on the gamma frequency, with a sharp increase of more than 10 Hz from -40 %  $g_{Na}$  to -30%. It sharply decreases nearing baseline, at which increased  $g_{Na}$  of basket cells had very little effect on the gamma frequency (3.8, bottom left).

The effects of potassium on gamma frequency seems to more random without a clear trend in in- or decrease of conductance for all cell types. Each increment of 0.1 appeared to have a different effect on the gamma frequency, with some conditions showing a sharp increase or decrease in Hz. The power of the gamma frequency stayed mostly within the 35.5 to 37.5 Hz range (3.8, bottom right).

### 3.3.5 Theta-gamma power

Another aspect of the sodium-potassium experiment was a power analysis of the theta and gamma oscillations in the network based on the power spectrum density. The power of the theta and gamma oscillations were calculated from the local field potential (LFP) for the duration of the simulation (5000 ms) and are shown in figure 3.9. The figure is again split in both sodium and potassium conductance modifications for each cell type (pyramidal = blue, OLM = red, basket = cyan).

#### Theta power

Theta power showed an rising trend in all three cell types where O-LM and basket cells had the most significant increase in power in below-baseline conditions. This change in power occurred predominantly in the -50 % to -30 %  $g_{Na}$  range. After which, O-LM falls off together with the modified pyramidal condition and decreases slightly. The basket cell condition shows the relative highest theta power above baseline conditions and remained slightly above baseline (3.9, top left).

In the modified potassium conductance conditions only the pyramidal modifications had an almost linear increase in theta power from -50 % to +50 %  $g_K$ . Modifications in the other cell types remained fairly constant in theta power (3.9, top right).

#### Gamma power

Unlike the frequency, the power of the gamma oscillations showed a large spike in power when the O-LM cells were modified from -50 % to -40 %  $g_{Na}$  of almost double the power. The effect of which in the LFP power spectrum is visualized using a fast-Fourier transformation in figure 3.10. From this figure, it is clear that some conditions cause significant shifts in gamma power at specific frequencies (30–40 Hz and 60–70 Hz). The gamma power sharply drops back to a more constant level from baseline onwards. The other cell types show a shift from 1 and 0 Hz to 0 and 1 Hz for Pyramidal and Basket cell modified conditions respectively (3.9, bottom left).

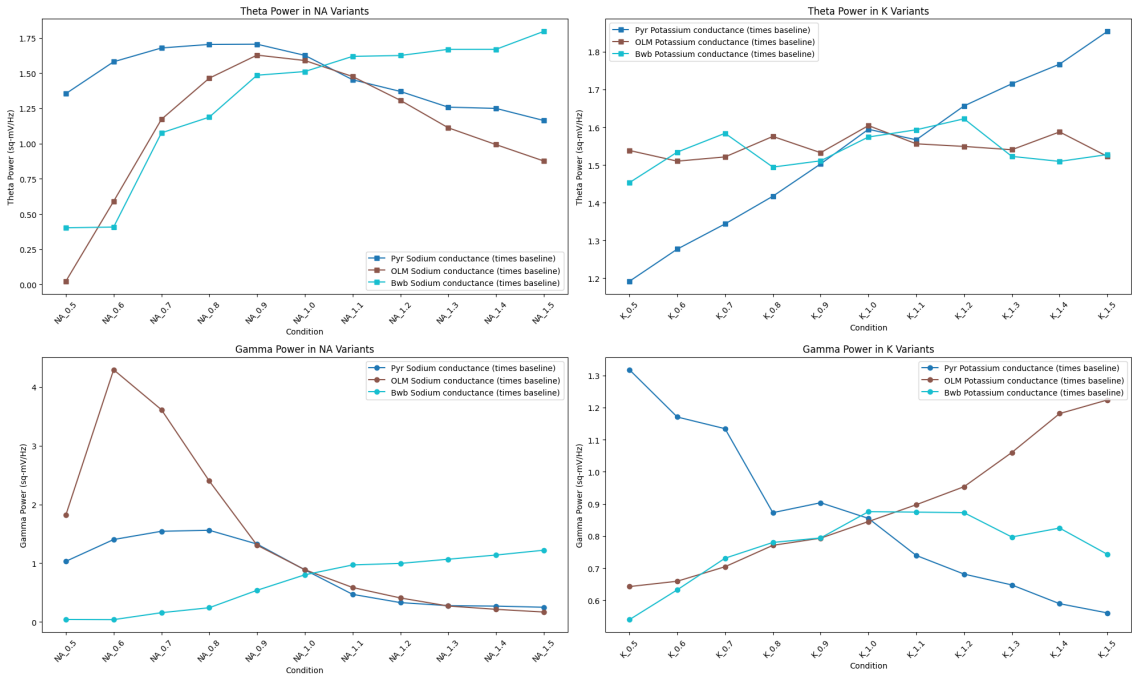


**Figure 3.9:** Sodium-Potassium variants: Theta-Gamma power.

The above figure shows the power of the theta and gamma oscillations in the network for each modified cell type. Each of the three cell types either had modified sodium or potassium conductance (pyr = blue, OLM = red, basket = cyan). The power of the theta and gamma oscillations were calculated from the local field potential (LFP) for the duration of the simulation (5000 ms). The x-axis represents the percentage amount of changed sodium or potassium conductance, times the baseline. The y-axis represents the theta and gamma power (in  $\text{mV}^2 \text{ Hz}^{-1}$ ).

Increased  $g_K$  of O-LM cells from -50 % onwards resulted in a constant rise in gamma power in the network, whereas modifications in pyramidal populations resulted in a steady decrease in gamma power. Basket cell modifications had a more random effect on gamma power, with some more extreme conditions reduced gamma power compared to baseline (3.9, bottom right).

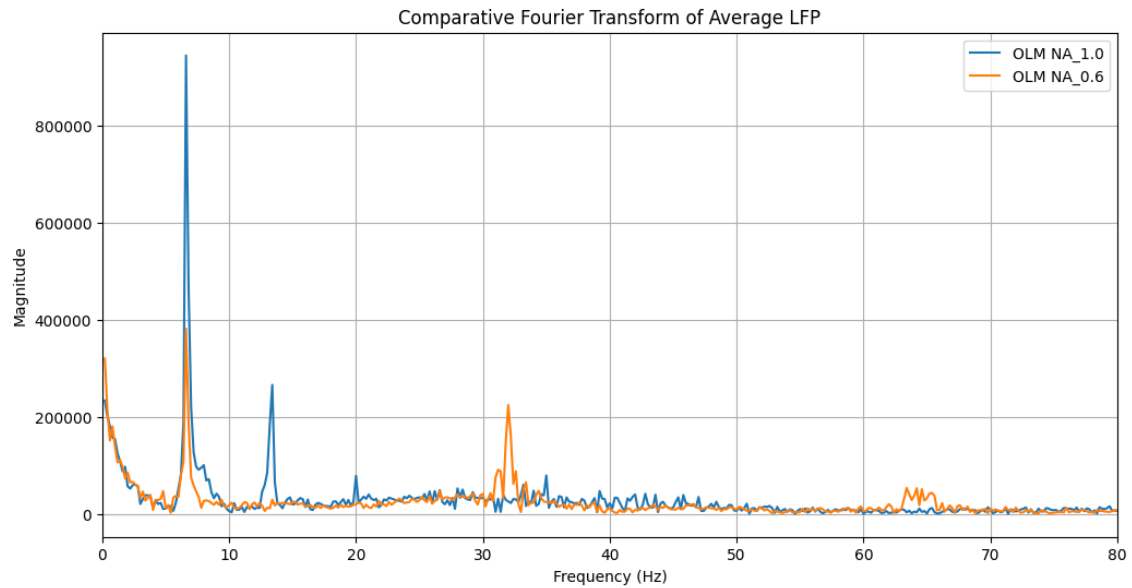


**Figure 3.10:** Comparative FFT of the LFP for OLM variants. The magnitude of the LFP is in arbitrary units. The signal is plotted for the frequency range that includes both theta and gamma in a range of 0 to 80 Hz. Blue is the baseline LFP, whereas orange represents a -40 % sodium conductance variant of O-LM cells.

## 3.4 Results of the External Noise variants

Building on the experiment of the sodium-potassium experiment, the network's sensitivity to a range of external noise conditions was tested for different combinations of modified pyramidal sodium/potassium conductance. The occurrence of depolarization block events in basket cells were quantified, including the average delay of these events in trials where they occurred. The external noise fed to the pyramidal cells was modified in increments of 0.05, ranging from 0.65 to 0.95 times the baseline noise level.

*More noise conditions are available for review in appendix C.*

### 3.4.1 Occurrence of depolarization block events across noise conditions

To test the susceptibility of the network to depolarization block (DPB) events, the percentage of trials where DPB events occurred was calculated in figure 3.11. The color intensity of the matrices indicate how often the network entered an epileptic state per noise condition for different combinations of pyramidal cell modifications of sodium and potassium. In matrix a in figure 3.11, there were barely any DPB events in the 15 trials per condition. Most of the DPB events occurred near baseline  $g_{\text{Na}}$  and  $g_{\text{K}}$  conditions and with elevated  $g_{\text{K}}$  only. In matrix b, the number of DPB events increased significantly, with the most events occurring at elevated pyramidal sodium conductance conditions. Matrix c showed a similar trend to matrix b, with more DPB events occurring also at more severely elevated pyramidal potassium conductance conditions. Matrix d showed the most DPB events, with the most events occurring at elevated pyramidal sodium conductance conditions with the exception of severely reduced sodium and potassium conductance combinations (bottom left). The selected noise levels are a percentage of the fixed 20x times baseline external noise level (0.65, 0.75, 0.85, 0.95).

### 3.4.2 Average delay of depolarization block events across noise conditions

The average delay (+ standard deviation) of depolarization block (DPB) events was calculated in trials where these events occurred in figure 3.12. These matrices showed similar trends to the DPB percentage matrices, with the average delay of DPB events being the shortest in the conditions where the most DPB events occurred. These same conditions are associated with the the shortest average delay of DPB events and least standard deviation (3.12, c and d). The selected noise ranges are the same as in the percentage matrices, a percentage of the fixed 20x times baseline external noise level (0.65, 0.75, 0.85, 0.95).

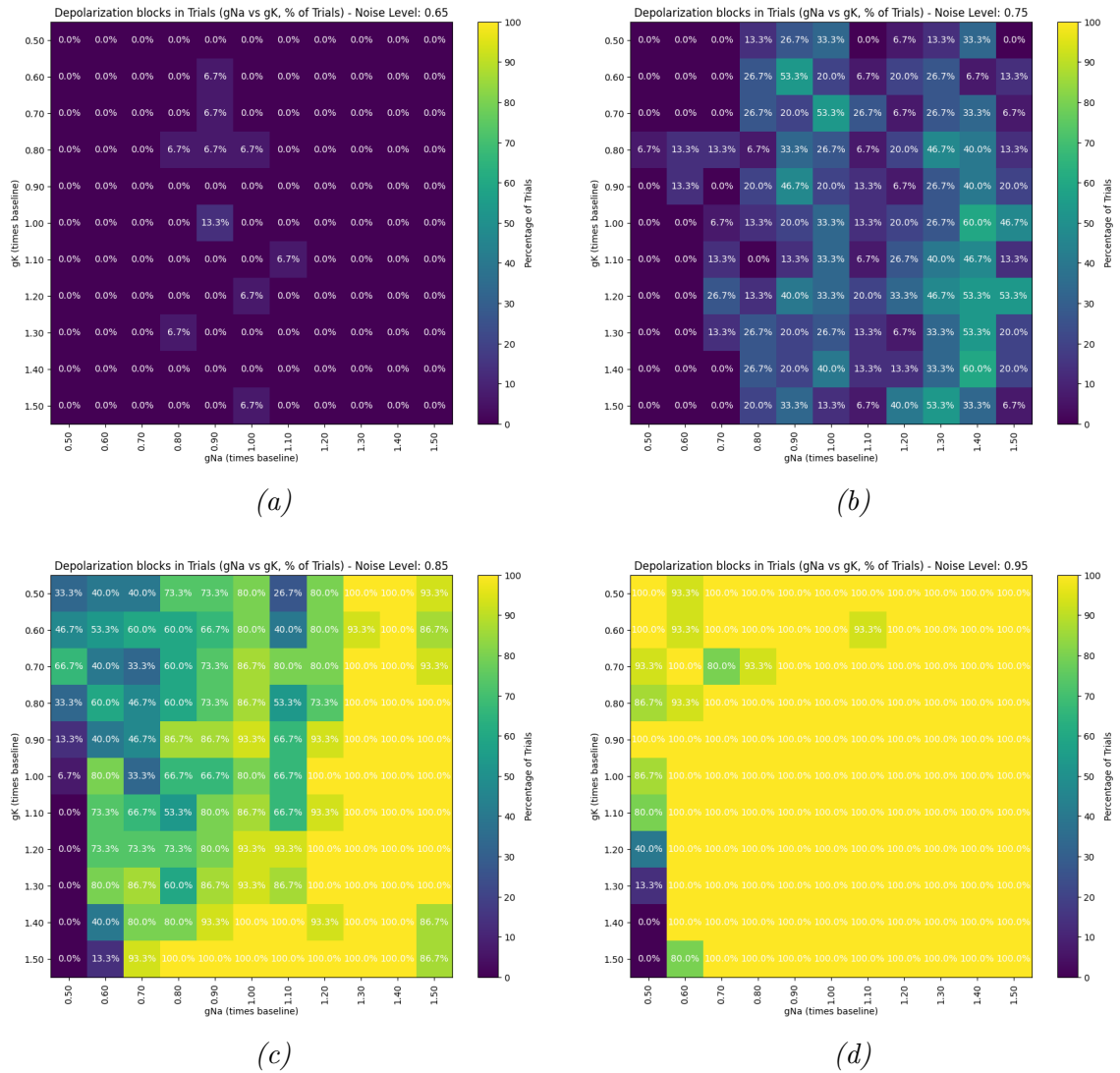


**Figure 3.11:** Percentage of trials where depolarization block events occurred for all tested noise conditions. The x-axis shows all the sodium conductance changes in pyramidal cells, whereas the y-axis shows the potassium conductance changes in pyramidal cells. Modifications to pyramidal cells were applied to all compartments. The color intensity scales from 0 to 100 %, where high-intensity yellow equals a higher amount of DPB events in a condition. The images are labeled from low noise to higher noise (a through d), respectively.

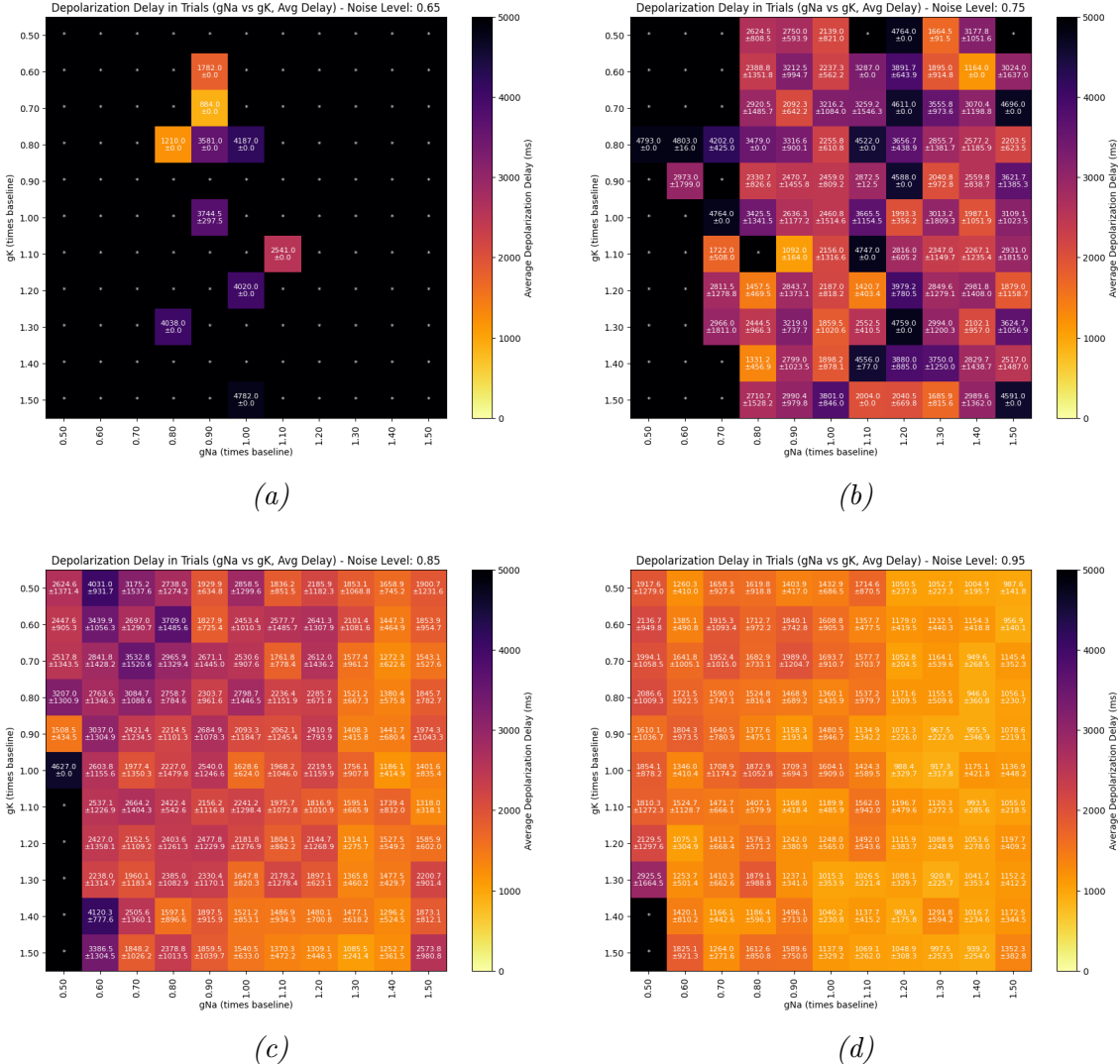


**Figure 3.12:** Average delay + Standard deviation of DPB in trials where depolarization block events occurred for all tested noise conditions. The x-axis shows all the sodium conductance changes in pyramidal cells, whereas the y-axis shows the potassium conductance changes in pyramidal cells. Modifications to pyramidal cells were applied to all compartments. The color intensity shows the average delay, where high-intensity red equals a shorter delay in DPB events in a condition. An asterisk (\*) is an indication that no DPB events occurred in the condition and is colorless. The images are labeled from low noise to higher noise (a through d), respectively.

## 3.5 Results of the External Noise: Burst analysis

In addition to the depolarization block (DPB) analysis, the population bursts of pyramidal and basket neurons were analyzed near the onset of a DPB event. Both peak height and general shape of the bursts were visualized in figure 3.13. The 2nd to last before, last burst before and 1st burst after the DPB event were detected and analyzed. A range of sodium:potassium conductance changes in pyramidal cells were tested, namely: 1.00–1.00, 0.80–1.20, 1.20–0.80, and 1.20–1.20. The external noise was fixed at 20x times the baseline of the original model. Each burst has been aligned relative to the onset of the burst of the pyramidal population in the network (ms). The bursts were averaged over 15 trials, and the standard deviation of the spike activity was visualized as a filled gradient surrounding the curve.

### 3.5.1 Inter-ictal state

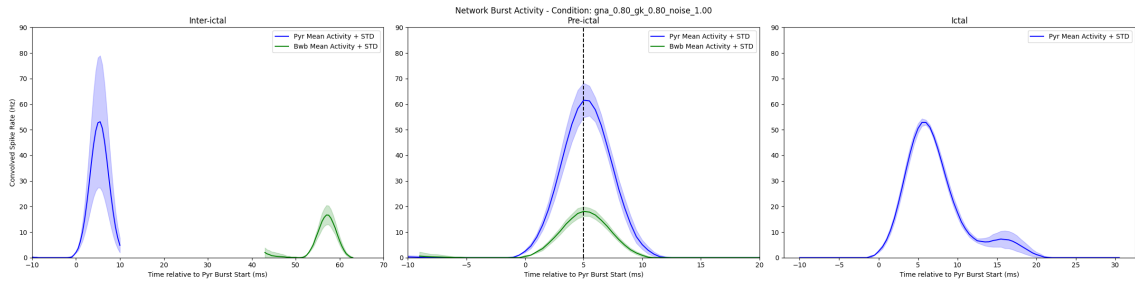
For the baseline condition, in the inter-ictal state the 2nd to last burst before the depolarization block was detected. The basket cell population burst occurred slightly before the pyramidal population burst with fairly low variance (3.13, a). In all other conditions the basket cell burst occurred at least 50 ms after the pyramidal population burst. The size of the basket cell burst only showed more variance in the 0.80–0.80 sodium:potassium condition (3.13, d), where the pyramidal burst also showed the most size variance.

### 3.5.2 Pre-ictal state

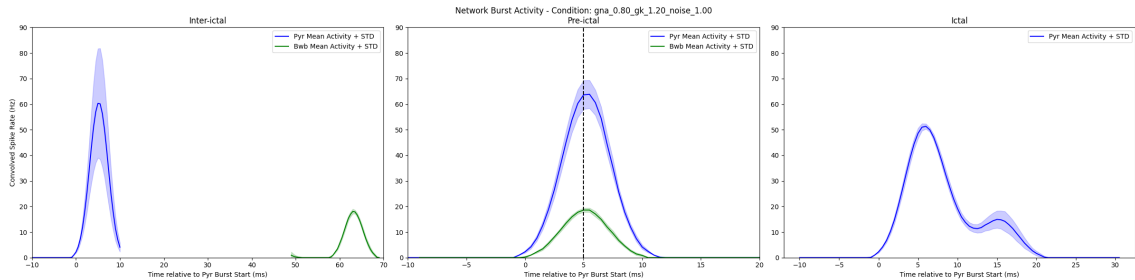
The pre-ictal network state shows the last burst before the depolarization block. From the Sanjay et al. (2015) article, large external drive from the pyramidal population blocks basket cell firing. Thus, the shift in basket cell burst timing is expected to be ahead of the pyramidal burst compared in the pre-ictal state. In the baseline condition the pyramidal burst peaks right after the basket cell burst (3.13, a). However, in all other conditions the basket cell burst shifts to further after the pyramidal burst, with the largest shift in the 1.20–1.20 sodium:potassium condition (3.13, e). Again, the variance if the basket cell burst was very small compared to the pyramidal population (which is also four times larger than the basket cell population)

### 3.5.3 Ictal state

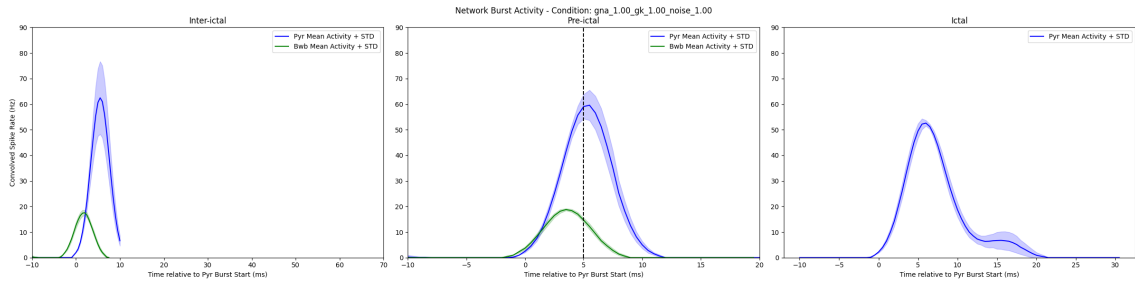
The ictal network state shows the first burst after the depolarization block, which only contained pyramidal activity in all conditions. The shape of the pyramidal burst was fairly consistent across all conditions, in the 1.20–0.80 sodium:potassium condition the burst variance was slightly larger (3.13, c). In addition this particular pyramidal burst lost its secondary peak, which was present in all other conditions. All other conditions showed a secondary peak in the pyramidal burst, as the population spike activity became more desynchronized due to lack of somatic inhibition by the flat-lined basket cell activity (example of such population activity is visible in figure 2.4). The height of the pyramidal burst peak stayed consistent across all conditions.



(a)

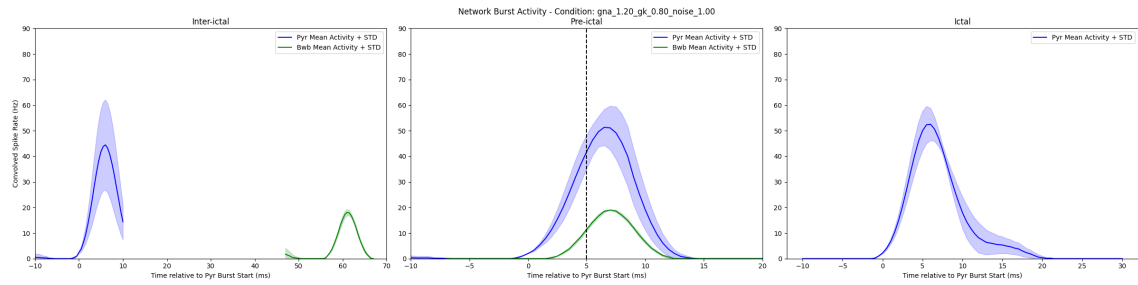


(b)

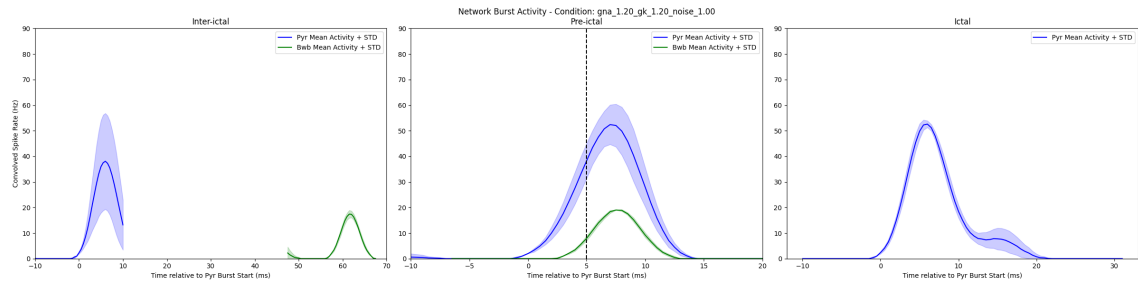


(c)

**Figure 3.13:** Burst detection near the onset of a depolarization block. Shows the 2nd to last burst before the DPB (inter-ictal, left), the last burst before the DPB (pre-ictal, middle), and the first burst after the DPB (ictal, right). The bursts are aligned relative the the onset of the burst of the pyramidal population in the network (ms). The curve of the spike burst shows the standard deviation of the spike activity as a filled gradient surrounding the curve. A horizontal dashed black line was added to the pre-ictal plot to more easily compare the shift in burst timing for the basket population. Y-axes were normalized across all conditions. The bursts of both pyramidal neurons (blue) and basket cells are shown (green).



(d)



(e)

### 3.6 Results of the Recurrent Connections variants

In this experiment, it was investigated if the network's susceptibility for depolarization block (DPB) events (ictal state) could be reduced by modifying the recurrent connection strength of basket cells. The effects of stronger recurrent connections of basket cells was tested in conditions of sodium:potassium conductance combinations of pyramidal cells (+- 25 %  $g_{Na}$  or  $g_K$ ). Steps of 5 % increased recurrent connection strength were tested, ranging from 1.00 to 1.15 times the baseline connection strength (figure 3.14).

At baseline, all conditions showed the maximum amount of DPB events in the network (figure 3.14: a, 15 out of 15 trials or 100 %). Increasing the recurrent connection strength of basket cells by 5 % led to slight decrease in the amount of DPB events in the network in 4 out of the 9 tested conditions (figure 3.14: b). At 10 % increased recurrent connection strength, the amount of DPB events decreased much strongly and some of the severe conditions only have DPB events in less than half of the trials (figure 3.14: c). Lastly, at 15 % increased recurrent connection strength, the amount of DPB events decreased even further, with some conditions showing no DPB events at all (figure 3.14: d).

*More noise conditions are available for review in appendix C.*

LEFT OF HERE, maybe add some numerical information to all the results sections?

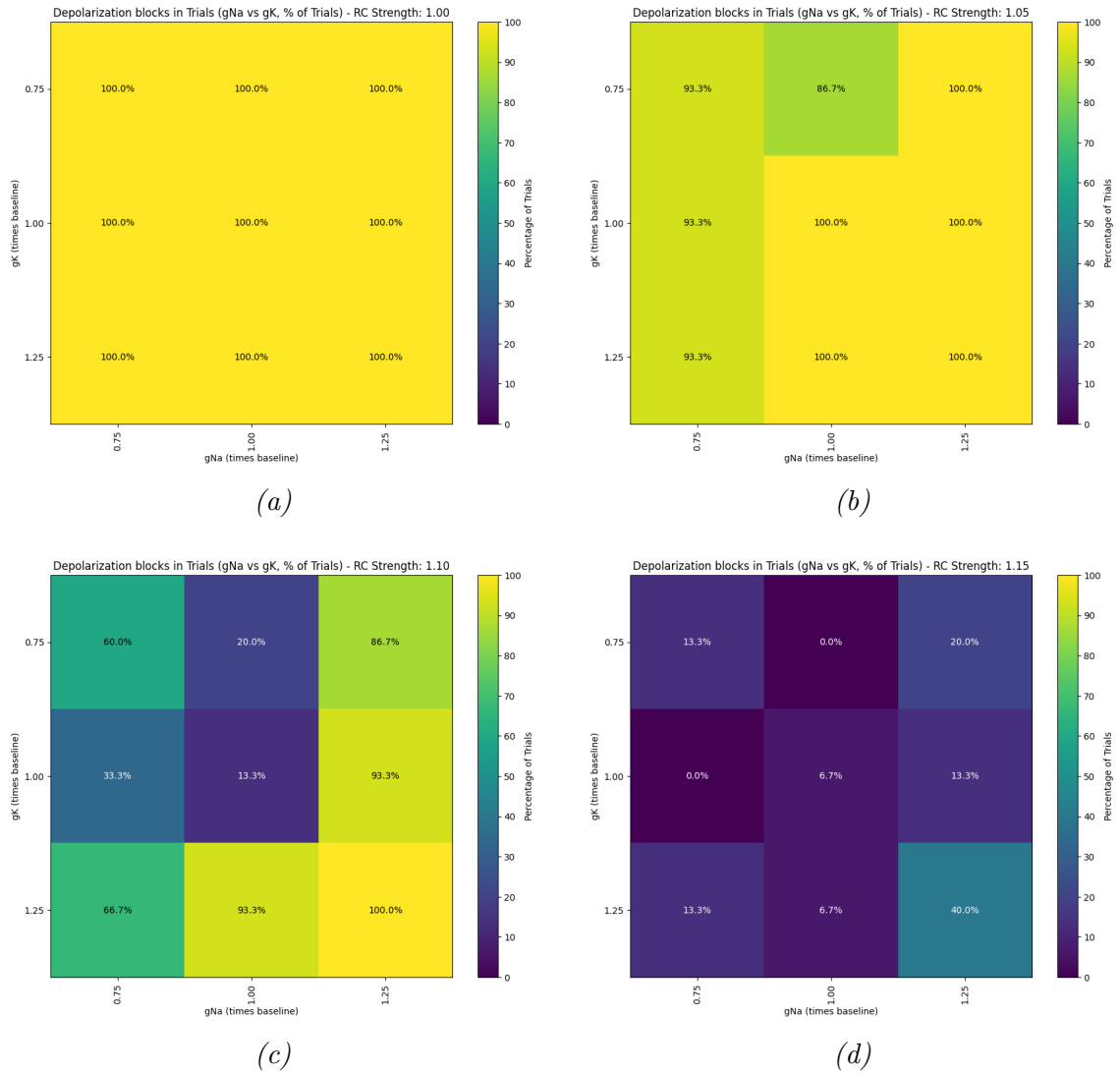


**Figure 3.14:** Percentage of trials where depolarization block events occurred for all tested noise conditions. The x-axis shows all the sodium conductance changes in pyramidal cells, whereas the y-axis shows the potassium conductance changes in pyramidal cells. Modifications to pyramidal cells were applied to all compartments. The color intensity shows the average delay, where high-intensity yellow equals higher percentage of DPB events in a condition. The images are labeled from low noise to higher noise (a through d), respectively.

# **4 Discussion**

This chapter holds the discussion of the results and the implications of the findings. It also includes the limitations of the research and suggestions for future research.

- 4.1 Discussion of the results**
- 4.2 Implications of the findings**
- 4.3 Limitations of the research**
- 4.4 Suggestions for future research**

# A Appendix

## A.1 Cellular dynamics: equations and parameters

The mathematical formulations of the cell types below are based on the work of Sanjay et al. (2015) and have been implemented as published in their model release on GitHub in the relevant NEURON mod files.

**Basket cells:** The transient sodium current was described by

$$I_{Na,I} = g_{Na,I} m_\infty^3 h (V_I - E_{Na,I}),$$

where

$$m_\infty = \frac{\alpha_m}{\alpha_m + \beta_m},$$

and

$$\alpha_m(V_I) = -0.1 \frac{(V_I + 35)}{e^{-0.1(V_I+35)} - 1}, \quad \beta_m(V_I) = 4e^{-\frac{(V_I+60)}{18}}.$$

The inactivation variable  $h$  obeyed the first-order kinetics:

$$\frac{dh}{dt} = \phi(\alpha_h(1 - h) - \beta_h h),$$

where

$$\alpha_h(V_I) = 0.07e^{-\frac{(V_I+58)}{20}}, \quad \beta_h(V_I) = \frac{1}{e^{-0.1(V_I+28)} + 1}.$$

The delayed rectifier potassium current was described by

$$I_{K,I} = g_{K,I} n^4 (V_I - E_{K,I}),$$

where the activation variable  $n$  obeyed the following equation:

$$\frac{dn}{dt} = \phi(\alpha_n(1 - n) - \beta_n n),$$

with

$$\alpha_n(V_I) = -0.01 \frac{(V_I + 34)}{e^{-0.1(V_I+34)} - 1}, \quad \beta_n(V_I) = 0.125e^{-\frac{(V_I+44)}{80}}.$$

For the experiments, the following parameters were used:  $g_{Na,I} = 35 \text{ mS/cm}^2$ ,  $g_{K,I} = 9 \text{ mS/cm}^2$ ,  $E_{Na,I} = 55 \text{ mV}$ ,  $E_{K,I} = -90 \text{ mV}$ ,  $\phi = 5$ .

**O-LM cells:** The channel currents were described by

$$I_{Na,o} = g_{Na,o} m^3 h (V_O - E_{Na,O}),$$

where  $m$  obeyed

$$\frac{dm}{dt} = \alpha_m(1-m) - \beta_m m,$$

with

$$\alpha_m = \frac{-0.1(V_O + 38)}{e^{\frac{-(V_O + 38)}{10}} - 1}, \quad \beta_m = 4e^{-\frac{(V_O + 65)}{18}},$$

and  $h$  obeyed

$$\frac{dh}{dt} = \alpha_h(1-h) - \beta_h h,$$

with

$$\alpha_n(V_O) = 0.07e^{\frac{-(V_O + 63)}{20}}, \quad \beta_n(V_O) = \frac{1}{1 + e^{\frac{-0.1(V_O + 33)}{10}}},$$

Similarly,

$$I_{K,O} = g_{K,O} n^4 (V_O - E_{K,O}),$$

$$\frac{dn}{dt} = \alpha_n(1-n) - \beta_n n,$$

$$\alpha_n(V_O) = \frac{0.018(V_O - 25)}{1 - e^{-\frac{V_O - 25}{25}}}, \quad \beta_n(V_O) = \frac{0.0036(V_O - 35)}{e^{\frac{V_O - 35}{12}} - 1}$$

$$I_{h,O} = g_{h,O} r (V_O - E_{h,O}),$$

$$\frac{dr}{dt} = \frac{r_\infty - r}{\tau_r},$$

$$r_\infty(V_O) = \frac{1}{1 + e^{-\frac{V_O + 84}{10.2}}}, \quad \tau_r(V_O) = \frac{1}{e^{-14.59 - 0.086V_O} + e^{-1.87 + 0.0701V_O}};$$

$$I_{A,O} = g_{A,O} ab (V_O - E_{A,O}),$$

$$\frac{da}{dt} = \frac{\alpha_\infty - a}{\tau_a},$$

$$\alpha_\infty(V_O) = \frac{1}{1 + e^{\frac{-(V_O + 14)}{16.6}}}, \quad \tau_a(V_O) = 5,$$

$$\frac{db}{dt} = \frac{b_\infty - b}{\tau_b},$$

$$b_\infty(V_O) = \frac{1}{1 + e^{\frac{V_O + 71}{7.3}}}, \quad \tau_b(V_O) = \frac{1}{\frac{0.000009}{e^{\frac{V_O - 26}{18.5}}} + \frac{0.014}{0.2 + e^{\frac{-(V_O + 70)}{11}}}}.$$

For the experiments, the following parameters were used:  $g_{Na,o} = 30 \text{ mS/cm}^2$ ,  $g_{K,O} = 23 \text{ mS/cm}^2$ ,  $g_{h,O} = 12 \text{ mS/cm}^2$ ,  $g_{A,O} = 16 \text{ mS/cm}^2$ ,  $E_{Na,O} = 90 \text{ mV}$ ,  $E_{K,O} = -100 \text{ mV}$ ,  $E_{h,O} = -32.9 \text{ mV}$ ,  $E_{A,O} = -90 \text{ mV}$ .

**Pyramidal cells:**  $I_{\text{conn},E_k}$  was the current due to electrical coupling between compartments, which was given by

$$I_{\text{conn},E,k} = g_{k,j+1}(V_{E,j+1} - V_{E,j}) + g_{k,j}(V_{E,j-1} - V_{E,j})$$

with the coupling conductance given by

$$g_{k,j} = \frac{r_k r_j^2}{R_a L_k (L_k r_j^2 + L_j r_k^2)}$$

where  $L_k$  and  $r_k$  was the length and radius of the compartment  $k$  respectively (note the need of units conversion in order to get  $g_{k,j}$  in mS/cm<sup>2</sup>). The ionic currents were given by:

$$\begin{aligned} I_{Na,E_k} &= g_{Na,E_k} m^3 h i (V_{E_k} - E_{Na,E}), \\ I_{K,E_k} &= g_{K,E_k} n^4 (V_0 - E_{K,E}), \\ I_{h,E_k} &= g_{h,E_k} r (V_{E_k} - E_{h,E}), \\ I_{A,E_k} &= g_{A,E_k} ab (V_{E_k} - E_{A,E}), \end{aligned}$$

and the gating variables obeyed equations of the form

$$\frac{dx}{dt} = \frac{x_\infty - x}{\tau_x},$$

where  $x = m, h, i, n, r, a, b$  and

$$m_\infty = \frac{\alpha_m}{\alpha_m + \beta_m}, \quad \tau_m = \max \left( 0.2, \frac{0.5}{\alpha_m + \beta_m} \right),$$

$$\begin{aligned} \alpha_m(V_{E_k}) &= \frac{0.4(V_{E_k} + 30)}{1 - e^{-\frac{V_{E_k} + 30}{7.2}}}, & \beta_m(V_{E_k}) &= \frac{0.124(V_{E_k} + 30)}{e^{\frac{V_{E_k} + 30}{7.2}} - 1}, \\ h_\infty(V_{E_k}) &= \frac{1}{1 + e^{\frac{V_{E_k} + 50}{4}}}, & \tau_h &= \max \left( 0.5, \frac{0.5}{\alpha_h + \beta_h} \right), \\ \alpha_h(V_{E_k}) &= \frac{0.03(V_{E_k} + 45)}{1 - e^{-\frac{V_{E_k} + 45}{1.5}}}, & \beta_h(V_{E_k}) &= \frac{0.01(V_{E_k} + 45)}{e^{\frac{V_{E_k} + 45}{1.5}} - 1}, \\ i_\infty(V_{E_k}) &= \frac{1 + b_k e^{\frac{V_{E_k} + 60}{2}}}{1 + e^{\frac{V_{E_k} + 60}{2}}}, & \tau_i &= \max \left( 10, \frac{30000 \beta_i}{1 + \alpha_i} \right), \\ \alpha_i(V_{E_k}) &= e^{0.45(V_{E_k} + 66)}, & \beta_i(V_{E_k}) &= e^{0.09(V_{E_k} + 66)}, \\ n_\infty &= \frac{1}{1 + \alpha_n}, & \tau_n &= \max \left( 2, \frac{50 \beta_n}{1 + \alpha_n} \right), \\ \alpha_n(V_{E_k}) &= e^{-0.11(V_{E_k} - 13)}, & \beta_n(V_{E_k}) &= e^{-0.08(V_{E_k} - 13)}, \end{aligned}$$

$$\begin{aligned}
r_{\infty, \text{HCN}2}(V_{E_k}) &= \frac{1}{1 + e^{\frac{V_{E_k} - V_{50k}}{10.5}}}, & \tau_{r, \text{HCN}2}(V_{E_k}) &= \frac{1}{e^{-14.59 - 0.086V_{E_k}} + e^{-1.87 + 0.0701V_{E_k}}}, \\
r_{\infty, \text{HCN}1}(V_{E_k}) &= \frac{1}{1 + e^{0.151(V_{E_k} - V_{50k})}}, & \tau_{r, \text{HCN}1}(V_{E_k}) &= \frac{e^{0.033(V_{E_k} + 75)}}{0.011(1 + e^{0.0833(V_{E_k} + 75)})}, \\
a_{\infty} &= \frac{1}{1 + \alpha_a}, & \tau_a &= \max\left(0.1, \frac{c_k \beta_a}{1 + \alpha_a}\right), \\
\alpha_a(V_{E_k}) &= e^{-0.038\left(d_k + \frac{1}{1 + \frac{e^{V_{E_k}} + 40}{e^{E_k} - 5}}\right)(V_{E_k} - e_k)}, & \beta_a(V_{E_k}) &= e^{-0.038\left(f_k + \frac{1}{1 + \frac{e^{V_{E_k}} + 40}{e^{E_k} - 5}}\right)(V_{E_k} - e_k)}, \\
b_{\infty}(V_{E_k}) &= \frac{1}{1 + e^{0.11(V_{E_k} + 56)}}, & \tau_b(V_{E_k}) &= \max(2, 0.26(V_{E_k} + 50)).
\end{aligned}$$

For the experiments, the following parameters were used:  $E_{Na, E_k} = 55$  mV,  $E_{K, E_k} = -90$  mV,  $E_{h, E_k} = -30$  mV,  $E_{A, E_k} = -90$  mV. The ionic conductances values (in mS/cm<sup>2</sup>) and values of other parameters dependent on the compartment are shown in the additional table section below.

# B Appendix

## B.1 Additional tables

### B.1.1 Sodium-Potassium variants numerical results.

**Table B.1:** Overview of results for the network with modified sodium conductance in pyramidal cells.

Pyr (Hz) + Std	BWB (Hz) + Std	OLM (Hz) + Std	Theta Freq (Hz)	Theta power (mV <sup>2</sup> Hz <sup>-1</sup> )	Gamma Freq (Hz)	Gamma power (mV <sup>2</sup> Hz <sup>-1</sup> )	Modified Celltype	Condition
1.33 ± 0.59	8.33 ± 1.98	0.69 ± 0.32	6.2	1.35	31.5	1.03	Pyr	0.5
1.47 ± 0.60	9.16 ± 1.97	0.79 ± 0.35	6.2	1.58	31.3	1.40	Pyr	0.6
1.59 ± 0.61	9.88 ± 2.08	0.87 ± 0.35	6.2	1.68	31.8	1.54	Pyr	0.7
1.69 ± 0.62	9.99 ± 2.19	0.94 ± 0.35	6.2	1.70	32.4	1.56	Pyr	0.8
1.77 ± 0.63	9.74 ± 2.16	1.00 ± 0.36	6.2	1.71	34.1	1.33	Pyr	0.9
1.87 ± 0.60	9.13 ± 2.26	1.06 ± 0.36	6.2	1.63	35.7	0.89	Pyr	1.0
2.00 ± 0.59	8.98 ± 2.32	1.14 ± 0.36	6.2	1.45	41.2	0.47	Pyr	1.1
2.11 ± 0.62	9.08 ± 2.56	1.23 ± 0.37	6.2	1.37	44.8	0.33	Pyr	1.2
2.17 ± 0.65	9.29 ± 2.67	1.29 ± 0.38	6.4	1.26	47.0	0.28	Pyr	1.3
2.21 ± 0.65	9.42 ± 2.67	1.37 ± 0.38	6.2	1.25	49.1	0.27	Pyr	1.4
2.25 ± 0.67	9.60 ± 2.69	1.41 ± 0.39	6.3	1.16	47.7	0.25	Pyr	1.5

**Table B.2:** Overview of results for the network with modified sodium conductance in basket cells.

Pyr (Hz) + Std	BWB (Hz) + Std	OLM (Hz) + Std	Theta Freq (Hz)	Theta power (mV <sup>2</sup> Hz <sup>-1</sup> )	Gamma Freq (Hz)	Gamma power (mV <sup>2</sup> Hz <sup>-1</sup> )	Modified Celltype	Condition
2.80 ± 0.65	0.00 ± 0.00	3.07 ± 0.43	7.8	0.40	34.2	0.04	Bwb	0.5
2.78 ± 0.65	0.02 ± 0.06	3.03 ± 0.44	7.8	0.41	33.9	0.04	Bwb	0.6
2.27 ± 0.69	3.54 ± 0.87	1.46 ± 0.40	6.4	1.08	46.9	0.16	Bwb	0.7
1.96 ± 0.62	7.37 ± 2.19	1.13 ± 0.36	6.2	1.19	45.0	0.24	Bwb	0.8
1.89 ± 0.60	8.39 ± 2.38	1.09 ± 0.36	6.2	1.49	38.8	0.54	Bwb	0.9
1.87 ± 0.60	9.07 ± 2.32	1.06 ± 0.36	6.2	1.51	37.0	0.80	Bwb	1.0
1.85 ± 0.60	9.57 ± 2.24	1.05 ± 0.36	6.2	1.62	35.8	0.97	Bwb	1.1
1.84 ± 0.59	9.61 ± 2.20	1.06 ± 0.36	6.2	1.63	36.5	1.00	Bwb	1.2
1.83 ± 0.60	9.79 ± 2.22	1.04 ± 0.36	6.2	1.67	37.0	1.07	Bwb	1.3
1.83 ± 0.60	10.08 ± 2.26	1.03 ± 0.36	6.2	1.67	35.1	1.14	Bwb	1.4
1.82 ± 0.59	10.30 ± 2.17	1.04 ± 0.35	6.2	1.80	36.2	1.22	Bwb	1.5

**Table B.3:** Overview of results for the network with modified sodium conductance in OLM cells.

Pyr (Hz) + Std	BWB (Hz) + Std	OLM (Hz) + Std	Theta Freq (Hz)	Theta power (mV <sup>2</sup> Hz <sup>-1</sup> )	Gamma Freq (Hz)	Gamma power (mV <sup>2</sup> Hz <sup>-1</sup> )	Modified Celltype	Condition
3.79 ± 1.00	18.76 ± 3.77	0.01 ± 0.03	4.0	0.02	37.8	1.82	OLM	0.5
3.22 ± 0.89	21.74 ± 2.41	0.23 ± 0.21	6.2	0.59	32.3	4.29	OLM	0.6
2.79 ± 0.80	18.51 ± 2.38	0.42 ± 0.26	6.2	1.17	32.8	3.61	OLM	0.7
2.45 ± 0.72	14.57 ± 2.40	0.62 ± 0.31	6.2	1.46	33.9	2.40	OLM	0.8
2.14 ± 0.67	11.20 ± 2.41	0.84 ± 0.34	6.2	1.63	34.9	1.31	OLM	0.9
1.87 ± 0.61	9.15 ± 2.26	1.06 ± 0.36	6.2	1.59	35.5	0.89	OLM	1.0
1.61 ± 0.55	7.49 ± 2.03	1.31 ± 0.38	6.2	1.48	37.7	0.59	OLM	1.1
1.36 ± 0.50	6.29 ± 1.84	1.60 ± 0.39	6.2	1.31	36.3	0.41	OLM	1.2
1.11 ± 0.45	4.98 ± 1.61	1.98 ± 0.39	6.2	1.11	35.6	0.27	OLM	1.3
0.90 ± 0.40	4.01 ± 1.38	2.49 ± 0.37	6.2	0.99	34.3	0.21	OLM	1.4
0.75 ± 0.36	3.31 ± 1.20	3.02 ± 0.35	6.2	0.88	36.7	0.17	OLM	1.5

**Table B.4:** Overview of results for the network with modified potassium conductance in pyramidal cells.

Pyr (Hz) + Std	BWB (Hz) + Std	OLM (Hz) + Std	Theta Freq (Hz)	Theta power (mV <sup>2</sup> Hz <sup>-1</sup> )	Gamma Freq (Hz)	Gamma power (mV <sup>2</sup> Hz <sup>-1</sup> )	Modified Celltype	Condition
2.15 ± 0.64	10.75 ± 2.43	1.32 ± 0.37	6.3	1.19	35.9	1.32	Pyr	0.5
2.05 ± 0.63	10.04 ± 2.34	1.25 ± 0.37	6.2	1.28	36.6	1.17	Pyr	0.6
1.97 ± 0.63	9.74 ± 2.33	1.14 ± 0.37	6.2	1.34	35.1	1.13	Pyr	0.7
1.93 ± 0.62	9.32 ± 2.48	1.11 ± 0.37	6.2	1.42	37.0	0.87	Pyr	0.8
1.90 ± 0.62	9.31 ± 2.29	1.08 ± 0.37	6.2	1.50	37.0	0.90	Pyr	0.9
1.86 ± 0.59	9.03 ± 2.24	1.07 ± 0.36	6.2	1.59	36.6	0.85	Pyr	1.0
1.83 ± 0.59	8.83 ± 2.26	1.05 ± 0.36	6.2	1.57	36.3	0.74	Pyr	1.1
1.79 ± 0.58	8.63 ± 2.17	1.03 ± 0.35	6.2	1.66	35.9	0.68	Pyr	1.2
1.75 ± 0.56	8.36 ± 2.16	1.02 ± 0.35	6.2	1.72	35.5	0.65	Pyr	1.3
1.72 ± 0.56	8.18 ± 2.04	1.00 ± 0.35	6.2	1.77	36.9	0.59	Pyr	1.4
1.68 ± 0.54	7.99 ± 2.08	0.99 ± 0.35	6.2	1.85	36.4	0.56	Pyr	1.5

**Table B.5:** Overview of results for the network with modified potassium conductance in basket cells.

Pyr (Hz) + Std	BWB (Hz) + Std	OLM (Hz) + Std	Theta Freq (Hz)	Theta power (mV <sup>2</sup> Hz <sup>-1</sup> )	Gamma Freq (Hz)	Gamma power (mV <sup>2</sup> Hz <sup>-1</sup> )	Modified Celltype	Condition
1.85 ± 0.58	9.19 ± 2.77	1.06 ± 0.36	6.2	1.45	36.6	0.54	Bwb	0.5
1.86 ± 0.59	9.11 ± 2.77	1.06 ± 0.36	6.2	1.53	37.0	0.63	Bwb	0.6
1.86 ± 0.60	9.12 ± 2.45	1.06 ± 0.36	6.2	1.58	36.8	0.73	Bwb	0.7
1.86 ± 0.60	9.06 ± 2.33	1.07 ± 0.36	6.2	1.49	36.6	0.78	Bwb	0.8
1.86 ± 0.60	8.94 ± 2.28	1.06 ± 0.36	6.2	1.51	36.7	0.79	Bwb	0.9
1.86 ± 0.60	9.07 ± 2.30	1.07 ± 0.36	6.2	1.57	36.0	0.88	Bwb	1.0
1.87 ± 0.60	9.07 ± 2.22	1.07 ± 0.36	6.2	1.59	36.2	0.87	Bwb	1.1
1.87 ± 0.61	9.03 ± 2.30	1.07 ± 0.38	6.2	1.62	35.7	0.87	Bwb	1.2
1.88 ± 0.61	8.93 ± 2.27	1.06 ± 0.36	6.2	1.52	36.9	0.80	Bwb	1.3
1.88 ± 0.61	8.86 ± 2.18	1.07 ± 0.36	6.2	1.51	37.0	0.82	Bwb	1.4
1.87 ± 0.61	8.71 ± 2.17	1.09 ± 0.36	6.2	1.53	37.7	0.74	Bwb	1.5

**Table B.6:** Overview of results for the network with modified potassium conductance in OLM cells.

Pyr (Hz) + Std	BWB (Hz) + Std	OLM (Hz) + Std	Theta Freq (Hz)	Theta power (mV <sup>2</sup> Hz <sup>-1</sup> )	Gamma Freq (Hz)	Gamma power (mV <sup>2</sup> Hz <sup>-1</sup> )	Modified Celltype	Condition
1.70 ± 0.57	8.01 ± 2.16	1.23 ± 0.36	6.2	1.54	38.8	0.64	OLM	0.5
1.73 ± 0.58	8.21 ± 2.13	1.19 ± 0.36	6.2	1.51	36.6	0.66	OLM	0.6
1.76 ± 0.58	8.34 ± 2.32	1.17 ± 0.37	6.2	1.52	37.4	0.70	OLM	0.7
1.79 ± 0.58	8.58 ± 2.17	1.14 ± 0.36	6.2	1.58	37.2	0.77	OLM	0.8
1.83 ± 0.59	8.81 ± 2.26	1.10 ± 0.36	6.2	1.53	35.9	0.79	OLM	0.9
1.87 ± 0.60	9.20 ± 2.26	1.07 ± 0.36	6.2	1.60	36.3	0.84	OLM	1.0
1.90 ± 0.61	9.40 ± 2.28	1.03 ± 0.36	6.2	1.56	36.1	0.90	OLM	1.1
1.94 ± 0.61	9.58 ± 2.30	1.00 ± 0.35	6.2	1.55	35.9	0.95	OLM	1.2
1.98 ± 0.63	9.99 ± 2.44	0.96 ± 0.36	6.2	1.54	36.1	1.06	OLM	1.3
2.02 ± 0.63	10.27 ± 2.30	0.93 ± 0.35	6.2	1.59	35.1	1.18	OLM	1.4
2.06 ± 0.65	10.66 ± 2.39	0.89 ± 0.35	6.2	1.52	35.4	1.22	OLM	1.5

## B.1.2 Compartment dependent parameters

**Table B.7:** Compartment dependent parameters used in the formulations of the three neuronal cell types. See A for the full equations. The ionic conductances are in mS/cm<sup>2</sup>.

	$g_h$	$g_A$	$g_{Na}$	$g_K$	$V_{50}$	$b$	$c$	$d$	$e$	$f$
Bdend	0.1	48	32	10	-82	1	4	1.5	11	0.825
Soma	0.1	48	32	10	-82	0.8	4	1.5	11	0.825
Adend1	0.2	72	32	10	-82	0.5	4	1.5	11	0.825
Adend2	0.4	120	32	10	-90	0.5	2	1.8	-1	0.7
Adend3	0.7	200	32	10	-90	0.5	2	1.8	-1	0.7

**Table B.8:** Synaptic Parameters for the Connectivity Between Neurons in the Model: Pre- and postsynaptic receptor types are given for each cell type. The time constants  $\tau_1$  and  $\tau_2$  are in milliseconds.  $\tau_1$  is the rise time constant, the time it takes for synaptic conductance to increase from baseline to peak.  $\tau_2$  is the decay time constant, the time it takes for the conductance to decrease from peak to baseline. The conductance indicates the strength of the synaptic connection and its ability to conduct ionic current across the postsynaptic membrane. This influences the extent to which the synaptic input can depolarize the postsynaptic neuron and is in nanoSiemens (nS).

Presynaptic	Postsynaptic	Receptor	$\tau_1$ (ms)	$\tau_2$ (ms)	Conductance (nS)
Pyramidal	Pyramidal	AMPA	0.05	5.3	0.02
Pyramidal	Pyramidal	NMDA	15	150	0.004
Pyramidal	Basket	AMPA	0.05	5.3	0.36
Pyramidal	Basket	NMDA	15	150	1.38
Pyramidal	OLM	AMPA	0.05	5.3	0.36
Pyramidal	OLM	NMDA	15	150	0.72
Basket	Pyramidal	GABA-A	0.07	9.1	0.72
Basket	Basket	GABA-A	0.07	9.1	4.5
Basket	OLM	GABA-A	0.07	9.1	0.0288
OLM	Pyramidal	GABA-A	0.2	20	72
MS	Basket	GABA-A	20	40	1.6
MS	OLM	GABA-A	20	40	1.6

### B.1.3 Connections

**Note:** For all tables the weight values are given in microsiemens ( $\mu\text{S}$ ). The weight is converted by taking into account that  $1\text{e-}3$  is equivalent to  $1 \mu\text{S}$ .

**Table B.9:** Pyramidal to Basket Weave Basket and OLM NMDA Synaptic Connections. This table summarizes the count and scaled synaptic weights for NMDA receptor-mediated connections originating from pyramidal neurons. The “Scale” variable allows modulation of the connection strength in various experimental conditions. Each connection specifies the number of synapses (‘Count’) and the effective synaptic weight (‘Weight’) after scaling, targeting NMDA receptors at specific postsynaptic sites.

Connection	Count	Weight ( $\mu\text{S}$ )	Synapse
Pyr to Bwb NMDA	100	scale $\times 1.38$	somaNMDA
Pyr to OLM NMDA	10	scale $\times 0.7$	somaNMDA
Pyr to Pyr NMDA	25	scale $\times 0.004$	BdendNMDA

**Table B.10:** Pyramidal to Basket Weave Basket and OLM AMPA Synaptic Connections. Detailed here are the AMPA receptor-mediated synaptic connections from pyramidal neurons. The “Scale” factor is applied to the base synaptic weight to explore its effect on network dynamics. The “Count” column reflects the number of synaptic contacts, while the “Weight” column indicates the scaled weight, directed towards AMPA receptors at the soma or dendritic compartments.

Connection	Count	Weight ( $\mu\text{S}$ )	Synapse
Pyr to Bwb AMPA	100	scale $\times$ 0.36	somaAMPAf
Pyr to OLM AMPA	10	scale $\times$ 0.36	somaAMPAf
Pyr to Pyr AMPA	25	scale $\times$ 0.02	BdendAMPA

**Table B.11:** Basket Cell GABAergic Synaptic Connections. This table provides information on the GABA receptor-mediated synaptic connections between basket weave basket cells and other neuronal types. The “Scale” factor adjusts the base synaptic weight for experimental analysis. The “Count” indicates how many synaptic connections are made, and the “Weight” reflects the scaled synaptic efficacy, impacting inhibitory GABAergic transmission.

Connection	Count	Weight ( $\mu\text{S}$ )	Synapse
Bwb to Bwb GABA	60	scale $\times$ 4.5	somaGABAf
Bwb to Pyr GABA	50	scale $\times$ 0.72	somaGABAf
Bwb to OLM GABA	17	scale $\times$ 0.036	somaGABAf

**Table B.12:** OLM to Pyramidal GABAergic Synaptic Connections. Presented here are the details of GABA receptor-mediated inhibitory connections from OLM cells to pyramidal neurons. The `olm_to_pyr_weight` variable represents a specific scaling factor for these connections, potentially derived from experimental data. The “Count” column denotes the number of connections, and the “Weight” column shows the scaled synaptic strength affecting GABAergic signaling at distal dendritic sites.

Connection	Count	Weight ( $\mu\text{S}$ )	Synapse
OLM to Pyr GABA	20	<code>olm_to_pyr_weight</code> $\times$ 72	Adend2GABAs
OLM to Pyr GABA 2	10	<code>olm_to_pyr_weight</code> $\times$ 1.44	Adend2GABAs

### B.1.4 NetStim parameters

**Note:** For all tables the weight values are given in microsiemens ( $\mu\text{S}$ ). The weight is converted by taking into account that  $1e-3$  is equivalent to  $1 \mu\text{S}$ .

**Table B.13:** NetStim Parameters Summary for Pyramidal Cells. The “Number” of spikes for each stimulus is calculated using the formula  $(1e3/\text{Interval}) \cdot h.tstop$  where  $h.tstop$  is 5000 ms, adjusting based on the specified interval for each stimulus. The `pyr_noise_scale` is used in the *external noise variants* experiment. This results in a target number of spikes over the simulation period.

Stimulus	Interval (ms)	Noise	Weight ( $\mu\text{S}$ )	Target
Pyr 1	1	1	0.05	somaAMPAf
Pyr 2	1	1	$0.05 \cdot \text{pyr\_noise\_scale}$	Adend3AMPAf
Pyr 3	1	1	0.012	somaGABAf
Pyr 4	1	1	0.012	Adend3GABAf
Pyr 5	100	1	$6.5 \cdot \text{pyr\_noise\_scale}$	Adend3NMDA

**Table B.14:** Noise to OLM NetStim Parameters Summary. The “Number” of spikes for each stimulus is calculated using the formula  $(1e3/\text{Interval}) \cdot h.tstop$ , with  $h.tstop$  representing the simulation stop time in ms, adjusted based on the specified interval for each stimulus. Different seeds are used for each stimulus instance.

Stimulus	Interval (ms)	Noise	Weight ( $\mu\text{S}$ )	Target
OLM 1	1	1	0.0625	somaAMPAf
OLM 2	1	1	0.2	somaGABAf

**Table B.15:** Noise to BWB NetStim Parameters Summary. The “Number” of spikes for each stimulus is calculated using the formula  $(1e3/\text{Interval}) \cdot h.tstop$ , where  $h.tstop$  is the simulation stop time in ms. Each stimulus is adjusted based on the specified interval. Different seeds are used for each stimulus instance to introduce variability.

Stimulus	Interval (ms)	Noise	Weight ( $\mu\text{S}$ )	Target
Bwb 1	1	1	0.02	somaAMPAf
Bwb 2	1	1	0.2	somaGABAf

**Table B.16:** Noise from MS to BWB & OLM NetStim Parameters Summary. The “Number” of spikes for each stimulus is calculated using the formula  $(1e3/\text{Interval}) \cdot h.tstop$ , with  $h.tstop$  representing the simulation stop time in ms. The specified interval for each stimulus defines the rate at which the NetStim will deliver spikes, with a non-random (noise=0) spike generation.

Stimulus	Interval (ms)	Noise	Weight ( $\mu\text{S}$ )	Target
OLM MS	150	0	1.6	somaGABA <sub>ss</sub>
Bwb MS	150	0	1.6	somaGABA <sub>ss</sub>

# C Appendix

## C.1 Additional data

## C.2 Additional figures

### C.2.1 External Noise variants: DPB percentage matrices

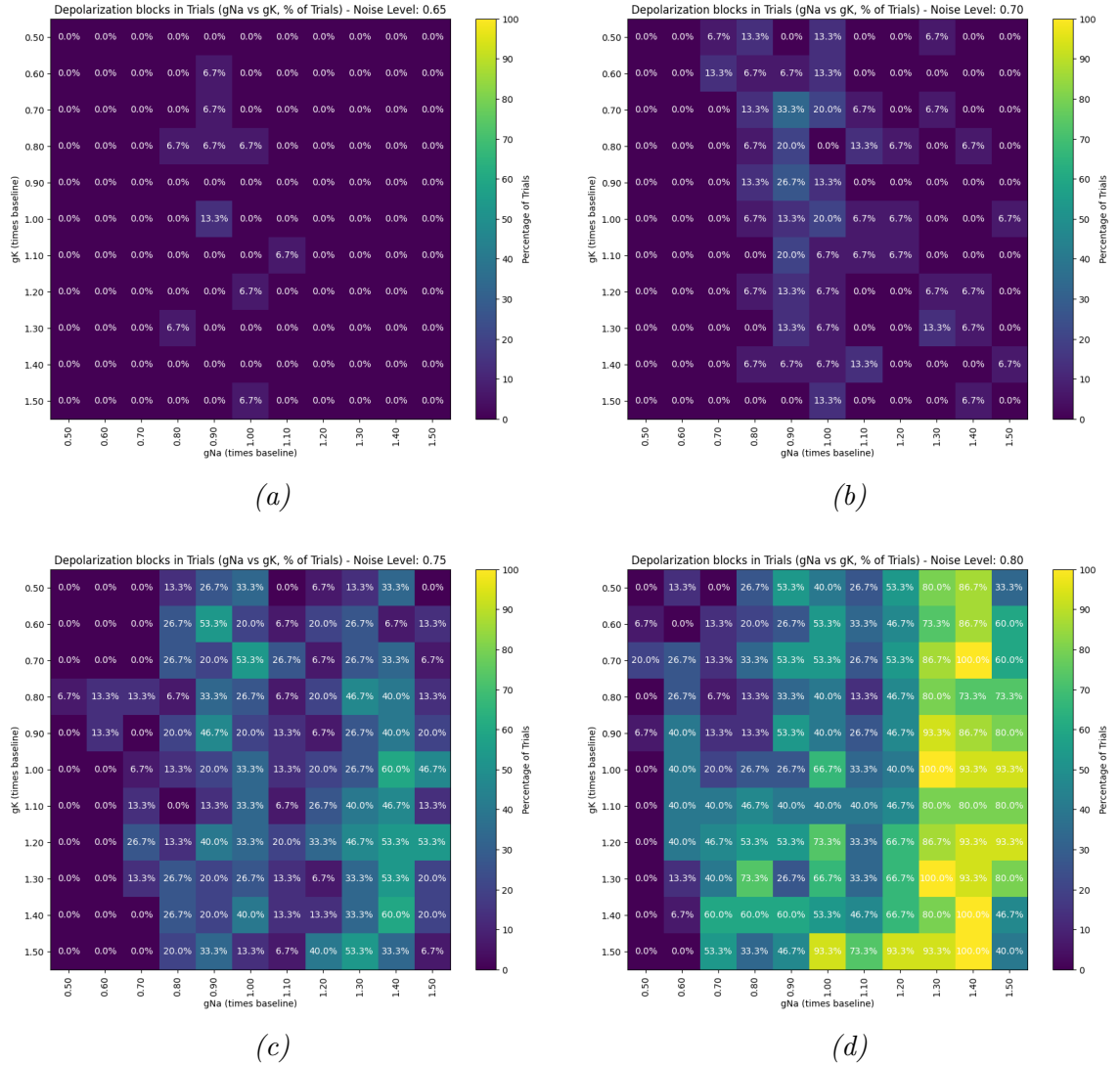
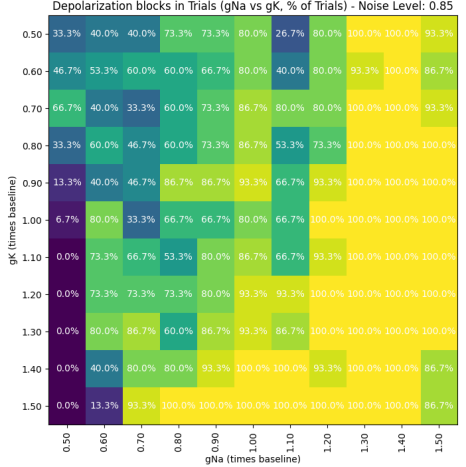
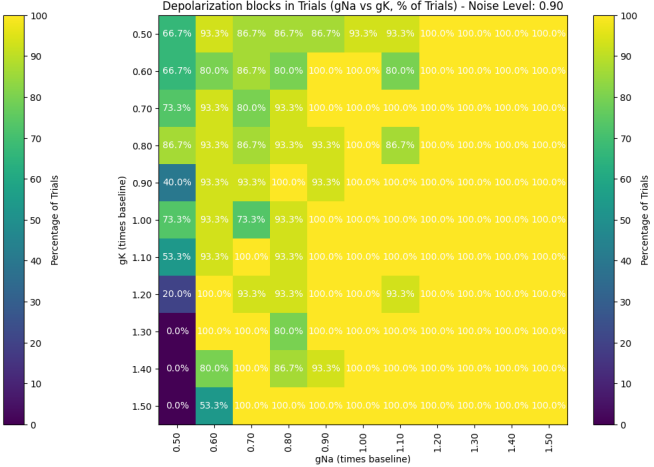


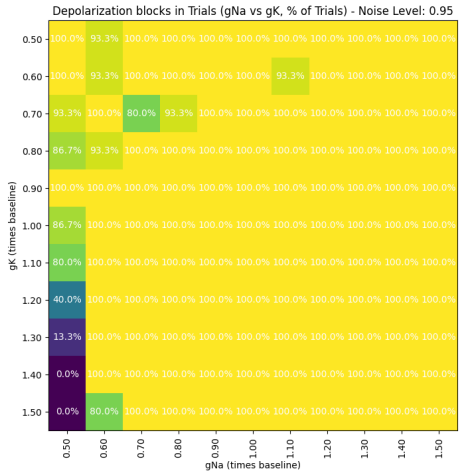
**Figure C.1:** Percentage of trials where depolarization block events occurred for all tested noise conditions. The x-axis shows all the sodium conductance changes in pyramidal cells, whereas the y-axis shows the potassium conductance changes in pyramidal cells. Modifications to pyramidal cells were applied to all compartments. The color intensity scales from 0 to 100 %, where high-intensity yellow equals a higher amount of DPB events in a condition. The images are labeled from low noise to higher noise (a through k), respectively.



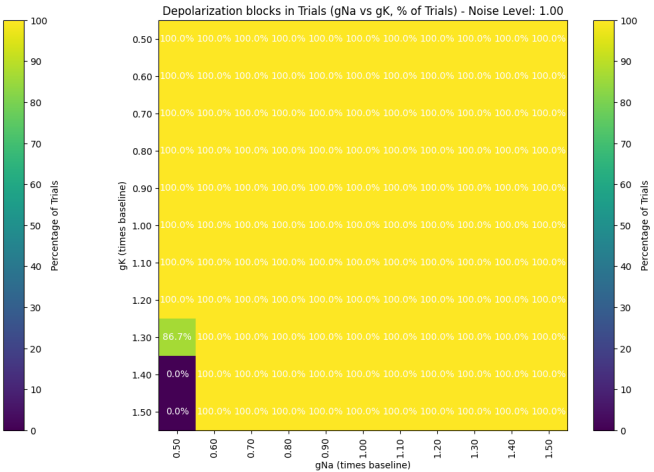
(e)



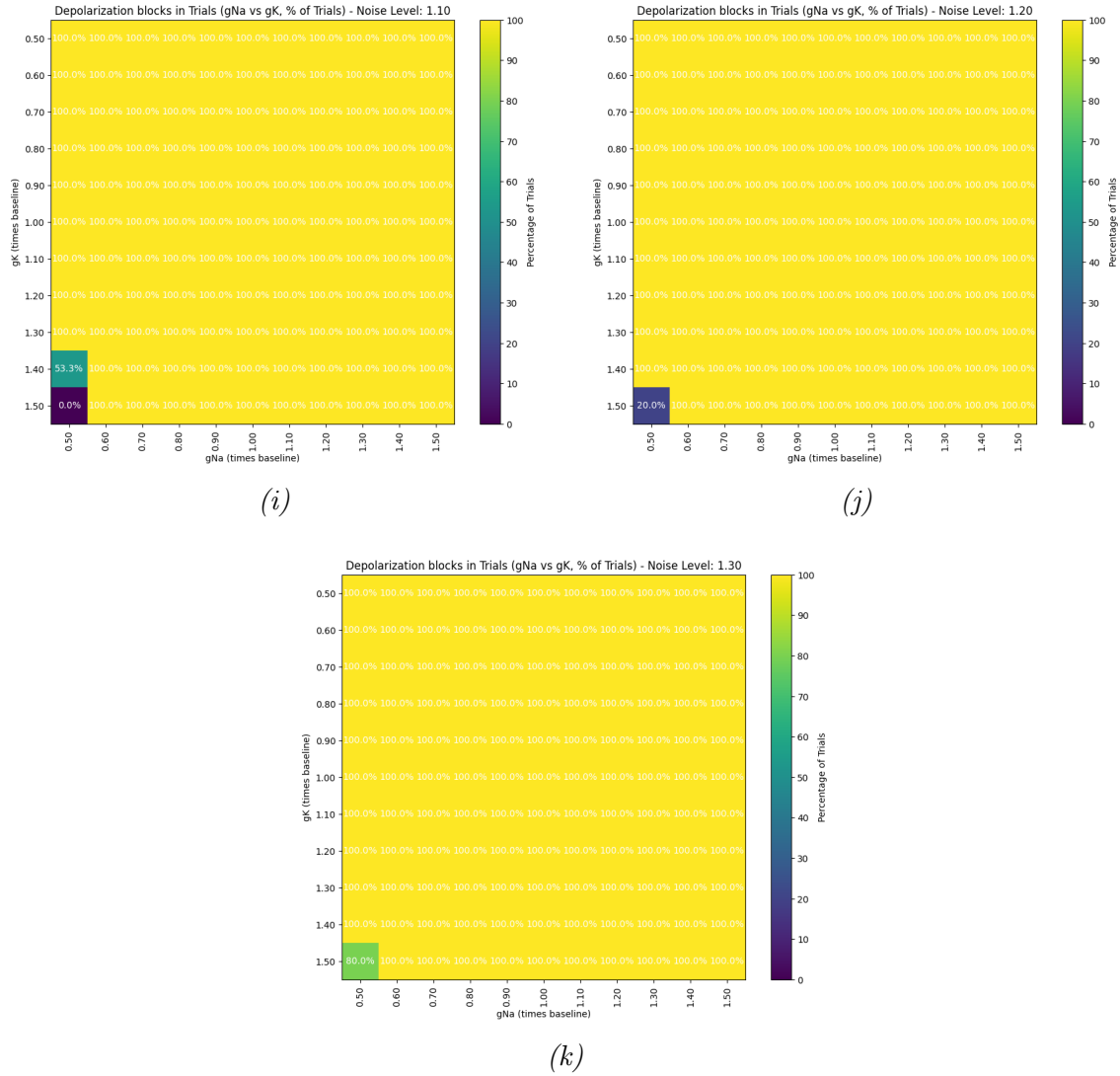
(f)



(g)



(h)



## C.2.2 External Noise variants: DPB delay matrices

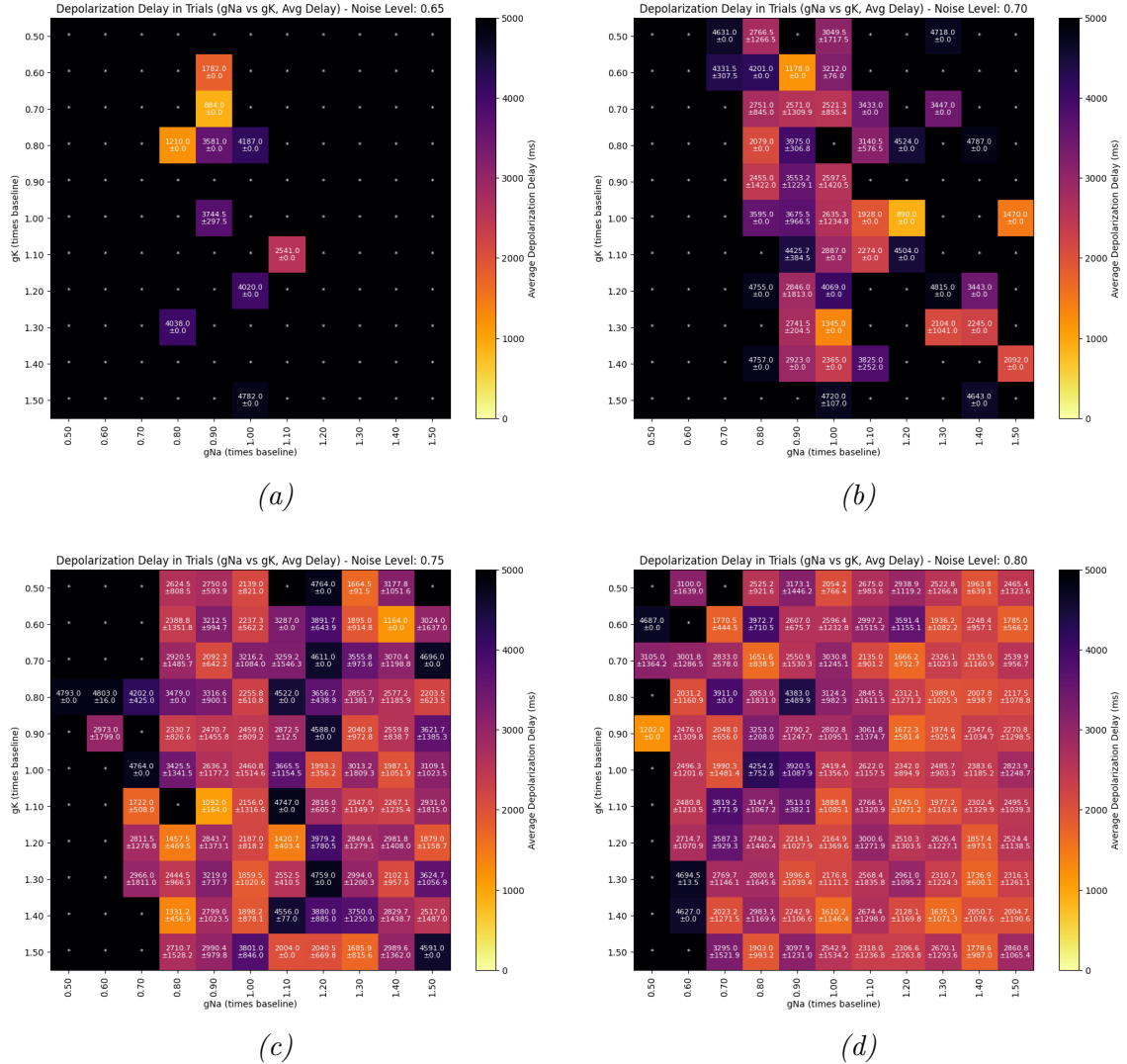
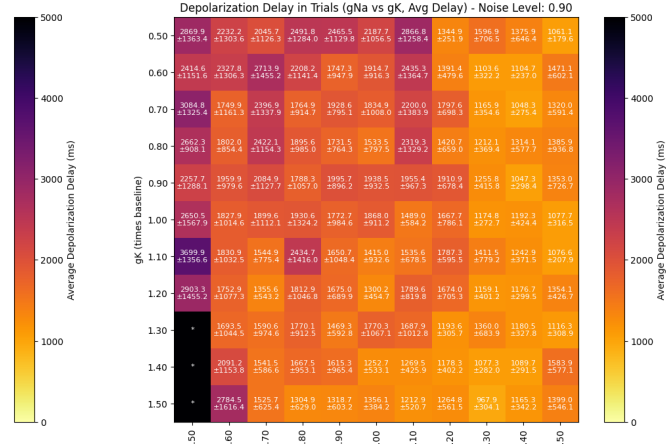


**Figure C.2:** Average delay + Standard deviation of DPB in trials where depolarization block events occurred for all tested noise conditions. The x-axis shows all the sodium conductance changes in pyramidal cells, whereas the y-axis shows the potassium conductance changes in pyramidal cells. Modifications to pyramidal cells were applied to all compartments. The color intensity shows the average delay, where high-intensity red equals a shorter delay in DPB events in a condition. An asterisk (\*) is an indication that no DPB events occurred in the condition and is colorless. The images are labeled from low noise to higher noise (a through k), respectively.

Depolarization Delay in Trials (gNa vs gK, Avg Delay) - Noise Level: 0.85



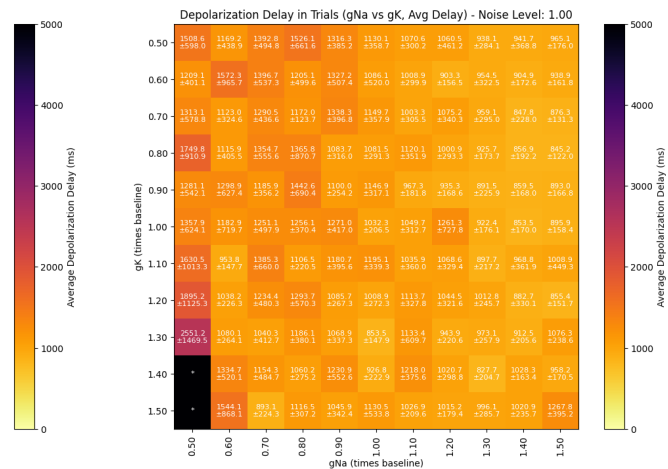
(e)

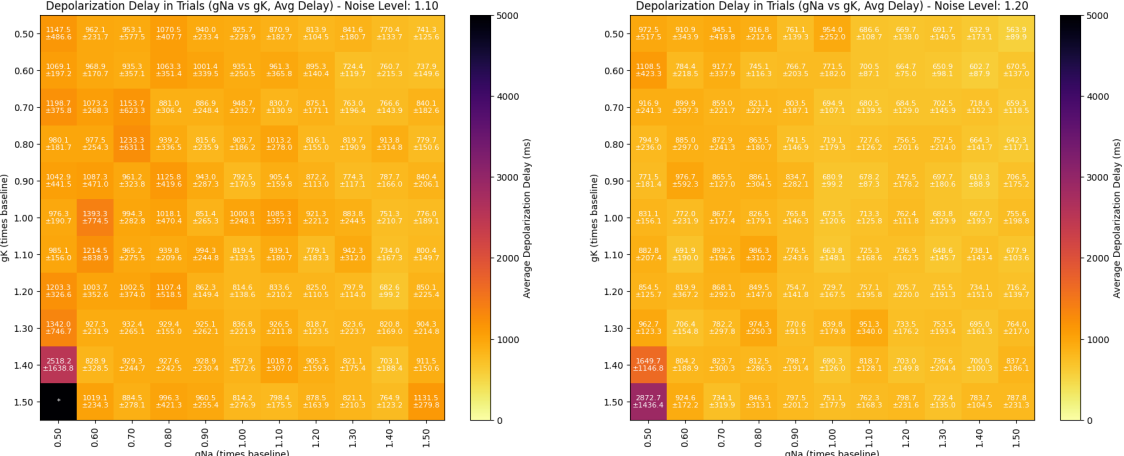


(f)



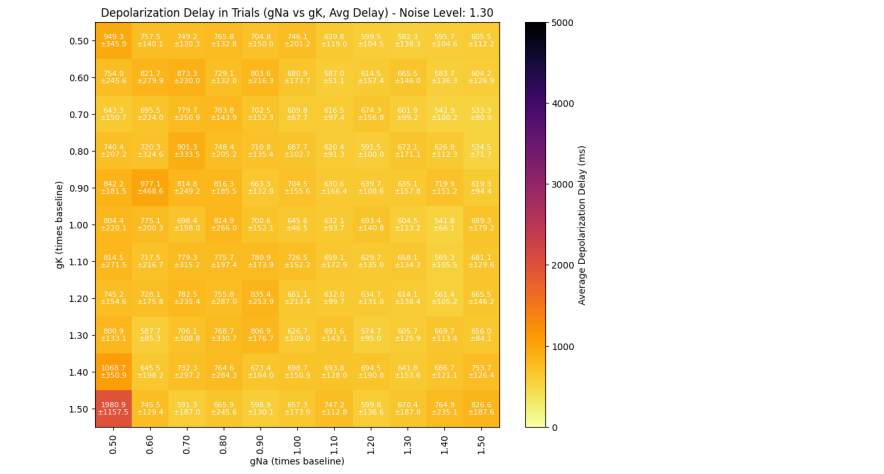
(g)





(i)

(j)



(k)



### C.2.3 Recurrent connection matrices

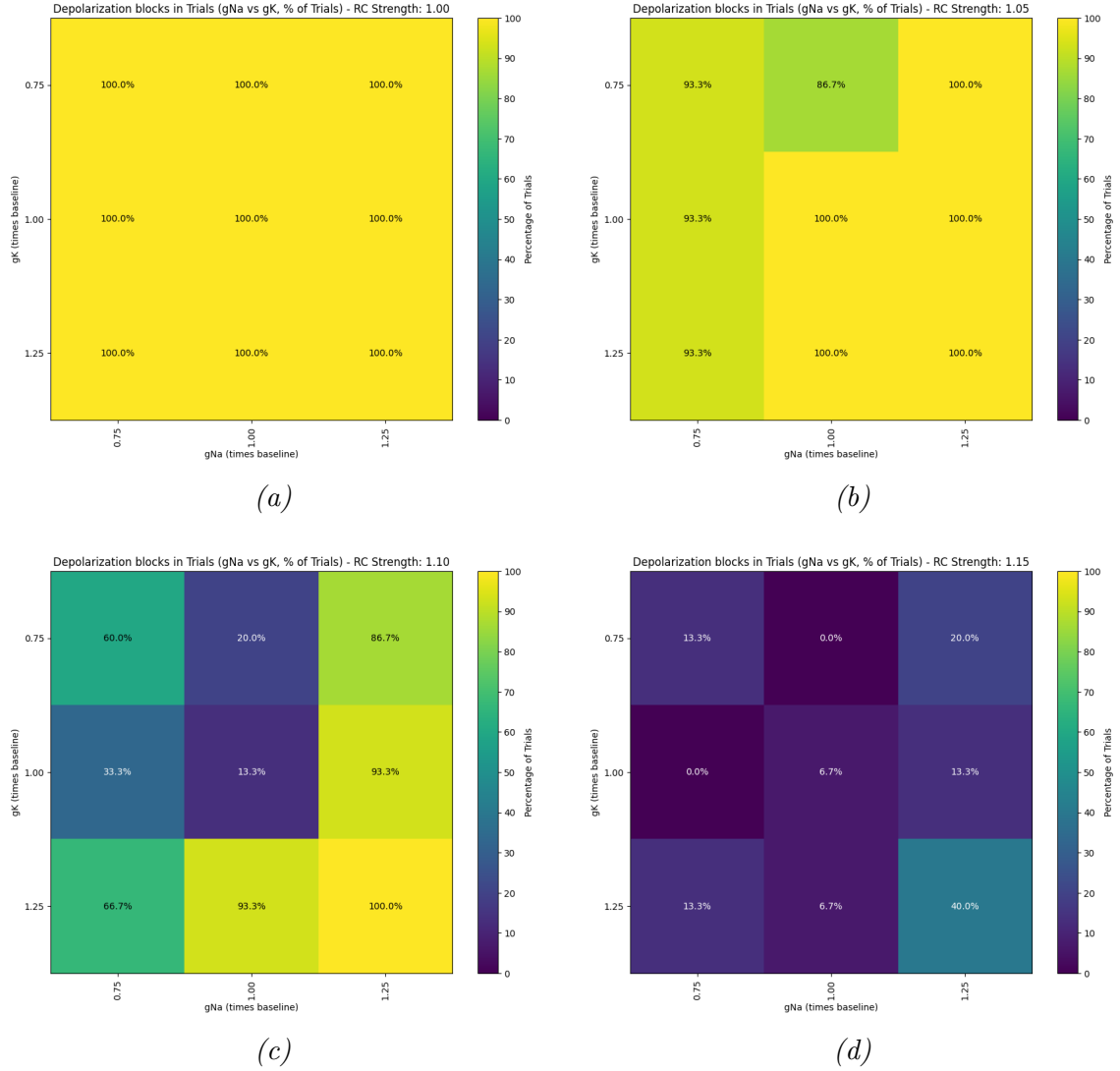
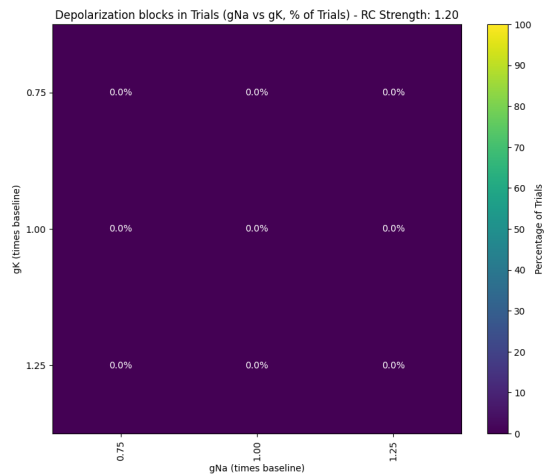


**Figure C.3:** Percentage of trials where depolarization block events occurred for all tested noise conditions. The x-axis shows all the sodium conductance changes in pyramidal cells, whereas the y-axis shows the potassium conductance changes in pyramidal cells. Modifications to pyramidal cells were applied to all compartments. The color intensity shows the average delay, where high-intensity yellow equals higher percentage of DPB events in a condition. The images are labeled from low noise to higher noise (a through e), respectively.



(e)

# Bibliography

- Aldenkamp, A. P., & Arends, J. (2004). Effects of epileptiform EEG discharges on cognitive function: Is the concept of “transient cognitive impairment” still valid? *Epilepsy & Behavior*, 5, 25–34. <https://doi.org/10.1016/j.yebeh.2003.11.005>
- Arski, O. N., Young, J. M., Smith, M.-L., & Ibrahim, G. M. (2021). The Oscillatory Basis of Working Memory Function and Dysfunction in Epilepsy. *Frontiers in Human Neuroscience*, 14. <https://doi.org/10.3389/fnhum.2020.612024>
- Brunklaus, A., & Lal, D. (2020). Sodium channel epilepsies and neurodevelopmental disorders: From disease mechanisms to clinical application. *Developmental Medicine & Child Neurology*, 62(7), 784–792. <https://doi.org/10.1111/dmcn.14519>
- Fisher, R. S., Acevedo, C., Arzimanoglou, A., Bogacz, A., Cross, J. H., Elger, C. E., Engel Jr, J., Forsgren, L., French, J. A., Glynn, M., Hesdorffer, D. C., Lee, B., Mathern, G. W., Moshé, S. L., Perucca, E., Scheffer, I. E., Tomson, T., Watanabe, M., & Wiebe, S. (2014). ILAE Official Report: A practical clinical definition of epilepsy. *Epilepsia*, 55(4), 475–482. <https://doi.org/10.1111/epi.12550>
- Gao, K., Lin, Z., Wen, S., & Jiang, Y. (2022). Potassium channels and epilepsy. *Acta Neurologica Scandinavica*, 146(6), 699–707. <https://doi.org/10.1111/ane.13695>
- Graves, T. (2006). Ion channels and epilepsy. *QJM: An International Journal of Medicine*, 99(4), 201–217. <https://doi.org/10.1093/qjmed/hcl021>
- Hodgkin, A. L., Huxley, A. F., & Katz, B. (1952). Measurement of current-voltage relations in the membrane of the giant axon of Loligo. *The Journal of Physiology*, 116(4), 424–448. Retrieved April 11, 2024, from <https://www.ncbi.nlm.nih.gov/pmc/articles/PMC1392219/>
- Kalitzin, S., Petkov, G., Suffczynski, P., Grigorovsky, V., Bardakjian, B. L., Lopes Da Silva, F., & Carlen, P. L. (2019). Epilepsy as a manifestation of a multistate network of oscillatory systems. *Neurobiology of Disease*, 130, 104488. <https://doi.org/10.1016/j.nbd.2019.104488>
- Lüders, H. O., Najm, I., Nair, D., Widdess-Walsh, P., & Bingman, W. (2006). The epileptogenic zone: General principles. *Epileptic Disorders: International Epilepsy Journal with Videotape*, 8 Suppl 2, S1–9.
- Lytton, W. W., Orman, R., & Stewart, M. (2005). Computer simulation of epilepsy: Implications for seizure spread and behavioral dysfunction. *Epilepsy & Behavior*, 7(3), 336–344. <https://doi.org/10.1016/j.yebeh.2005.06.011>
- Migliore, M., Cannia, C., Lytton, W. W., Markram, H., & Hines, M. L. (2006). Parallel network simulations with NEURON. *Journal of Computational Neuroscience*, 21(2), 119–129. <https://doi.org/10.1007/s10827-006-7949-5>

- Migliore, M., Messineo, L., & Ferrante, M. (2004). Dendritic Ih Selectively Blocks Temporal Summation of Un同步ized Distal Inputs in CA1 Pyramidal Neurons. *Journal of Computational Neuroscience*, 16(1), 5–13. <https://doi.org/10.1023/B:JCNS.0000004837.81595.b0>
- Neymotin, S. A., Lazarewicz, M. T., Sherif, M., Contreras, D., Finkel, L. H., & Lytton, W. W. (2011). Ketamine Disrupts Theta Modulation of Gamma in a Computer Model of Hippocampus. *Journal of Neuroscience*, 31(32), 11733–11743. <https://doi.org/10.1523/JNEUROSCI.0501-11.2011>
- Nyhus, E., & Curran, T. (2010). Functional role of gamma and theta oscillations in episodic memory. *Neuroscience & Biobehavioral Reviews*, 34(7), 1023–1035. <https://doi.org/10.1016/j.neubiorev.2009.12.014>
- Oyrer, J., Maljevic, S., Scheffer, I. E., Berkovic, S. F., Petrou, S., & Reid, C. A. (2018). Ion Channels in Genetic Epilepsy: From Genes and Mechanisms to Disease-Targeted Therapies (P. M. Sexton, Ed.). *Pharmacological Reviews*, 70(1), 142–173. <https://doi.org/10.1124/pr.117.014456>
- Sanjay, M., Neymotin, S. A., & Krothapalli, S. B. (2015). Impaired dendritic inhibition leads to epileptic activity in a computer model of CA3. *Hippocampus*, 25(11), 1336–1350. <https://doi.org/10.1002/hipo.22440>
- Saraga, F., Wu, C. P., Zhang, L., & Skinner, F. K. (2003). Active dendrites and spike propagation in multicompartment models of oriens-lacunosum/moleculare hippocampal interneurons. *The Journal of Physiology*, 552(3), 673–689. <https://doi.org/10.1113/jphysiol.2003.046177>
- Striano, P., & Minassian, B. A. (2020). From Genetic Testing to Precision Medicine in Epilepsy. *Neurotherapeutics*, 17(2), 609–615. <https://doi.org/10.1007/s13311-020-00835-4>
- Wang, X.-J., & Buzsáki, G. (1996). Gamma Oscillation by Synaptic Inhibition in a Hippocampal Interneuronal Network Model. *The Journal of Neuroscience*, 16(20), 6402–6413. <https://doi.org/10.1523/JNEUROSCI.16-20-06402.1996>
- Witter, M. P. (2007). Intrinsic and extrinsic wiring of CA3: Indications for connectional heterogeneity. *Learning & Memory*, 14(11), 705–713. <https://doi.org/10.1101/lm.725207>
- Yayik, A., Yildirim, E., Kutlu, Y., & Yildirim, S. (2015). Epileptic State Detection: Pre-ictal, Inter-ictal, Ictal. *International Journal of Intelligent Systems and Applications in Engineering*, 3(1), 14–18. <https://doi.org/10.18201/ijisae.14531>
- Yu, F. H., Mantegazza, M., Westenbroek, R. E., Robbins, C. A., Kalume, F., Burton, K. A., Spain, W. J., McKnight, G. S., Scheuer, T., & Catterall, W. A. (2006). Reduced sodium current in GABAergic interneurons in a mouse model of severe myoclonic epilepsy in infancy. *Nature Neuroscience*, 9(9), 1142–1149. <https://doi.org/10.1038/nn1754>